Projection-based reduced-order modelling of time-periodic problems, with application to flow past flapping hydrofoils

Lotz, Jacob E.; Weymouth, Gabriel D.; Akkerman, Ido

DOI
10.1016/j.cma.2024.117161

Publication date
2024

Document Version
Final published version

Published in
Computer Methods in Applied Mechanics and Engineering

Computer Methods in Applied Mechanics and Engineering 429 (2024) 117161

Contents lists available at ScienceDirect

Comput. Methods Appl. Mech. Engrg.

journal homepage: www.elsevier.com/locate/cma

Projection-based reduced-order modelling of time-periodic problems, with application to flow past flapping hydrofoils

Jacob E. Lotz *, Gabriel D. Weymouth, Ido Akkerman

Delft University of Technology, Faculty of Mechanical Engineering, P.O. Box 5, 2600 AA Delft, The Netherlands

ARTICLE INFO

Keywords:
Reduced-order model
Time-periodic
Space–time method
Galerkin-POD
Flapping foils
Variational multi-scale method

ABSTRACT

Simulating forced time-periodic flows in industrial applications presents significant computational challenges, partly due to the need to overcome costly transients before achieving time-periodicity. Reduced-order modelling emerges as a promising method to speed-up computations. We extend upon the work of Lotz et al. (2024) where a time-periodic space–time model is introduced. We present a time-periodic reduced-order model that directly finds the time-periodic solution without requiring extensive time integration. The reduced-order model gives a reduction in variables in both space and time. Our approach involves a POD-Galerkin reduced-order model based on a time-periodic full-order model that employs isogeometric analysis, residual-based variational multiscale turbulence modelling and weak boundary conditions. The projection-based reduced-order model inherits these features. We evaluate the reduced-order model with numerical experiments on moving hydrofoils. The motion is known a priori and we restrict ourselves to two spatial dimensions. In these experiments we vary the Strouhal and Reynolds numbers, and the motion profile respectively. Reduced-order model solutions agree well with those of the full-order model. The errors over the entire time period of thrust and lift forces are less than 0.2%. This includes complex scenarios such as the transition from drag to thrust production with increasing Strouhal number. Our time-periodic reduced-order model offers speed-ups ranging from $\mathcal{O}(10^2)$ to $\mathcal{O}(10^3)$ compared to the full-order model, depending upon the basis size. This makes it an appealing solution for prescribed time-periodic problems, with potential for additional speedup through nonlinear reduction techniques such as hyper-reduction.

1. Introduction

Finding a time-periodic solution of the flow past a prescribed periodically moving object using the Navier–Stokes equation is often associated with significant computational cost. Usually, a solution is found by integrating an initial condition over a sufficiently long time for a time-periodic solution to emerge. This transient phase usually consists of several periods. This makes these computations expensive in industrial applications, such as wind farm and propeller optimization. To overcome this problem, we explore the use of reduced-order models for speeding up this type of computations. Here, model assumptions or data are used to approximate the solution of the original model, the full-order model. In this work we focus on projection-based reduced-order models, where the full-order model is projected onto a reduced basis. This reduced basis is constructed from simulation data using proper orthogonal decomposition (POD). In this paper, we introduce a reduced-order model that directly solves the time-periodic solution, eliminating

* Corresponding author.
E-mail address: j.e.lotz@tudelft.nl (J.E. Lotz).

https://doi.org/10.1016/j.cma.2024.117161
Received 2 May 2024; Received in revised form 12 June 2024; Accepted 12 June 2024
Available online 21 June 2024

the need for time integration. By leveraging the advantages of a space–time discretization, where space and time are treated equally, we achieve a reduction in degrees of freedom in both space and time.

In the literature, various techniques are developed to obtain periodic solutions more efficiently. The shooting method is one of these methods [1–3]. It involves converting the time-periodic boundary value problem into an initial value problem. The objective is then to determine the correct initial condition that satisfies the original, possibly expensive, boundary value problem. Another cost-effective alternative is the spectral method [4,5]. The flow variables are represented by a Fourier series in time, facilitating the direct solution of periodic flows. This approach may face challenges in accurately capturing non-sinusoidal motion due to the rapid increase in the required number of Fourier modes. In the present study, we aim to develop an economical method for computing periodic solutions without assumptions on the motion. We use a time-periodic full-order model [6–9] to create a POD-Galerkin reduced-order model.

The stability of a reduced-order model is not guaranteed and a considerable amount of research is devoted to it. Instabilities of reduced-order models can be classified into at least two, and possibly more [10,11], classes: inf-sup instabilities, related to solving a saddle point problem, and instabilities due to convection-dominated flows. For the first class of instabilities, efforts have been made in velocity-only reduced-order models [12–14]. However, many numerical methods for obtaining the snapshots do not provide pointwise divergence-free flow fields [14,15], and neglecting the pressure term can lead to instabilities and large amplitude errors in the Galerkin model [16]. An attractive alternative is to enforce a solenoidal basis, which requires a Piola transform for data associated with essential boundary conditions [17]. For velocity-pressure reduced-order models, it is possible to enrich the velocity space with a supremizer, providing an additional set of degrees of freedom to solve for [18–21]. For instabilities of the second class, subgrid closure models are a promising approach. This involves the modelling of the eddy viscosity of the missing modes [22,23] or dynamic subgrid scales [24]. A successful alternative is the application of the variational multi-scale method [25] at both full-order and reduced-order model levels [10,26–28], which does not require additional supremizers or a solenoidal basis, as it provides an inf-sup stable model [10,26,29]. Alternatives to subgrid closure models can be found in e.g. data-driven techniques [21,30,31] or the use of neural networks [32–34]. We stabilize the reduced-order model with the variational multi-scale method, following the work in [26].

We first consider the full-order model, which is a variational multi-scale method [25] using isogeometric analysis [35] adapted for time-periodic space–time [9]. By solving the time domain monolithically, we are able to impose the time-periodic constraints a priori. We effectively transform the initial value problem into a boundary value problem. The dimension of the domain is increased by one, but it allows us to enforce the time-periodic constraint as a classic periodic boundary condition. The motion of the periodically moving object is considered known and is accommodated by appropriately shaping the space–time mesh in advance. We construct the reduced-order model by applying a Galerkin projection of the full-order model on a time-periodic basis. The basis is computed by means of a proper orthogonal decomposition of a snapshot matrix of which each entry is the entire periodic space–time solutions of the full-order model for a chosen parameter set. The resulting time-periodic reduced-order model, like the full-order model, directly computes the entire space–time solution. We evaluate the quality of the computed solution fields and forces by comparing them with the full-order model for three numerical experiments. The experiments evaluate the reduced-order model for a variation of the Strouhal number, Reynolds number or motion shape for a periodically moving hydrofoil in two dimensions. The first experiment is studied more elaborately. It examines the transition from drag to thrust production as the Strouhal number increases. For this experiment, we also study the effect of the basis size on solution quality and speed-up. In the last two experiments, we study the effect of the Reynolds number or motion shape on lift and drag.

2. Full-order and reduced-order model for the time-periodic incompressible flow

In this work, we transform the initial value problem into a boundary value problem. This is achieved by treating time analogously to space. Our notation reflects this analogy by disguising the time as an additional spatial dimension. Therefore, we directly obtain a time-periodic solution in both the full-order and reduced-order model. This approach eliminates the need for separate time integration. We use the space–time full-order model for periodic flow as described in [9].

For the reduced-order model, we consider a standard POD-Galerkin model. We are able to use this standard reduced order model as we effectively solve a boundary value problem. The reduced-order model gives a reduction of the number of variables in both spatial and temporal dimensions.

To provide a self-contained and reproducible work, we reproduce the strong formulation and discrete weak formulation of the model problem in the first two sections. For further details of the model, we refer to the original work.

2.1. Strong formulation of time-periodic incompressible flow

We consider incompressible flow on a periodically deforming domain $\Omega(t) = \Omega(t+T)$, where T is the period. We assume the unknown velocity $\mathbf{u}$ and pressure p exhibit the same periodicity, that is $\mathbf{u}(\mathbf{x},t) = \mathbf{u}(\mathbf{x},t+T)$ and $p(\mathbf{x},t) = p(\mathbf{x},t+T)$. The boundary is composed of an exterior part Γ_{ext} and a periodic time-dependent interior $\Gamma_{\text{int}}(t)$. We introduce the normal velocity $u_n = \mathbf{u}\cdot\mathbf{n}$ with positive and negative parts $u_n^{\pm} = \frac{1}{2}(u_n \pm |u_n|)$. The exterior boundary is further separated in an inflow and outflow part,

$$\Gamma_{\text{ext}}^{D} := \left\{\mathbf{x} \in \Gamma_{\text{ext}} | u_{\text{n}}(\mathbf{x}) < 0\right\}, \tag{1a}$$

$$\Gamma_{\text{ext}}^{N} := \left\{\mathbf{x} \in \Gamma_{\text{ext}} | u_{\text{n}}(\mathbf{x}) \geq 0\right\}, \tag{1b}$$

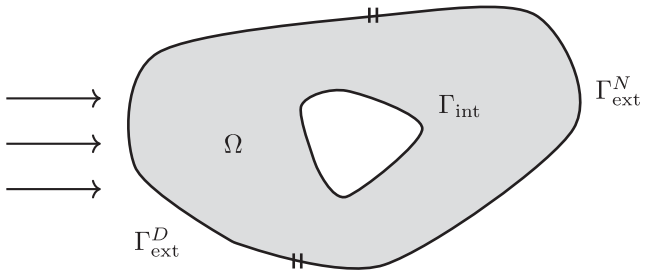

Fig. 1. Sketch of the spatial domain with its boundaries, with inflow on the left.

where the superscripts refer to the Dirichlet and Neumann boundary conditions that will be imposed on these parts.

Fig. 1 depicts a sketch of a spatial domain Ω, similar to the one we will consider in Section 3.

We extrude the spatial domain over the time domain $\mathcal{I} = [0, T]$ to obtain a continuous space–time domain Q with space–time boundaries P_{ext} and P_{int}. Here, $P_{\text{ext}} = \Gamma_{\text{ext}} \times \mathcal{I}$ while Q and P_{int} are deformed version of $\Omega \times \mathcal{I}$ and $\Gamma \times \mathcal{I}$ to accommodate the motion.

We denote the space–time coordinate, using the time direction $d+1$, as $\hat{\mathbf{x}}^T = [\mathbf{x}^T \; st] = [x_1 \; \dots \; x_d \; s x_{d+1}]$ and the extended velocity vector as $\hat{\mathbf{u}}^T = [\mathbf{u}^T \; s]$. Note that t is scaled with a reference velocity s to ensure dimensional consistency.

We substitute the traditional initial condition

$$\mathbf{u}(\cdot, 0) = \mathbf{u}_0(\cdot) \quad \text{in} \quad \Omega, \tag{2}$$

with its time-periodic counterpart

$$\mathbf{u}(\cdot, 0) = \mathbf{u}(\cdot, T) \quad \text{in} \quad \Omega, \tag{3}$$

which transforms an initial value problem into a boundary value problem. To make this point more clear we chose to denote the material derivative as

$$\partial_t \mathbf{u} + \mathbf{u} \cdot \nabla \mathbf{u} = \hat{\mathbf{u}} \cdot \nabla_{\hat{\mathbf{x}}} \mathbf{u}, \tag{4}$$

resulting in the Navier–Stokes equations for time-periodic incompressible flow,

$$\hat{\mathbf{u}} \cdot \nabla_{\hat{\mathbf{x}}} \mathbf{u} + \nabla p - \nu \nabla^2 \mathbf{u} = \mathrm{f} \qquad \text{in} \quad Q, \tag{5a}$$

$$\nabla \cdot \mathbf{u} = 0 \qquad \text{in} \quad Q, \tag{5b}$$

$$\mathbf{u} = \mathbf{u}^D_{\text{int}} \qquad \text{in} \quad P_{\text{int}}, \tag{5c}$$

$$\mathbf{u} = \mathbf{u}^D_{\text{ext}} \qquad \text{in} \quad P^D_{\text{ext}}, \tag{5d}$$

$$-p\mathbf{n} + \nu \nabla \mathbf{u} \cdot \mathbf{n} + u_{\text{n}}^{-} \mathbf{u} = \mathbf{0} \qquad \text{in} \quad P^N_{\text{ext}}, \tag{5e}$$

$$\mathbf{u}(\cdot, 0) = \mathbf{u}(\cdot, T) \quad \text{in} \quad \Omega, \tag{5f}$$

where ν is the kinematic viscosity, f is an external force and $\mathbf{u}^D_{\text{int}}$ and $\mathbf{u}^D_{\text{ext}}$ are prescribed velocities on the interior and exterior boundary.

The first two equations state the balance of linear momentum (5a) and mass (5b), respectively. Subsequently, the Dirichlet boundary conditions (5c) and (5d) prescribe the velocity on the interior and the inflow boundary. While (5e) governs the outflow boundary. Finally, (5f) enforces the time-periodic condition.

2.2. Discrete weak formulation of time-periodic incompressible flow

Converting the strong form, as given in the previous section, into a discrete formulation involves a couple of steps. First, we convert the strong form into a weak form, by multiplying the two balance equations with appropriate test-functions, integrating over the domain and applying integration by parts on the pressure and diffusion terms.

Subsequently, we discretize the formulation by decomposing the domain Q in non-overlapping elements Q_e. For ease of notation, we also define the union of element interiors as $\tilde{Q} = \bigcup Q_e$. We define simple polynomial (or rational) functions on each element and construct approximate function spaces, denoted as $\mathcal{W}^h$, by combining these appropriately.

Last, we stabilize the discrete formulation by accounting explicitly for the subgrid-scale effects. For this, we apply residual-based variational multiscale turbulence modelling as stabilization [25,36]. We split $\mathbf{u}$ and p into coarse-scale, denoted by ^{h}, and small-scale components, denoted with $'$,

$$\{\mathbf{u}, p\} = \left\{\mathbf{u}^h, p^h\right\} + \left\{\mathbf{u}', p'\right\}. \tag{6}$$

The small-scale components will be accounted for by a model.

For improved robustness, we choose to enforce the Dirichlet conditions weakly and added some residual-based discontinuity capturing. The resulting discrete variational formulation of (5) is similar to [9]. After these choices, the discrete problem is stated as follows:

Find $\boldsymbol{U}^h = \{\mathbf{u}^h, p^h\} \in \mathcal{W}^h$ *such that for all* $\boldsymbol{W} = \{\mathbf{w}^h, q^h\} \in \mathcal{W}^h$*:*

$$B\left(\boldsymbol{U}^h, \boldsymbol{W}^h\right) = 0, \tag{7a}$$

where

$$B\left(\boldsymbol{U}^h, \boldsymbol{W}^h\right) = B_{\mathrm{GAL}}\left(\boldsymbol{U}^h, \boldsymbol{W}^h\right) + B_{\mathrm{VMS}}\left(\boldsymbol{U}^h, \boldsymbol{W}^h\right) + B_{\mathrm{WBC}}\left(\boldsymbol{U}^h, \boldsymbol{W}^h\right) + B_{\mathrm{DC}}\left(\boldsymbol{U}^h, \boldsymbol{W}^h\right), \tag{7b}$$

$$B_{\mathrm{GAL}}\left(\boldsymbol{U}^h, \boldsymbol{W}^h\right) = \left(\mathbf{w}^h, \hat{\mathbf{u}}^h \cdot \nabla_{\hat{\mathbf{x}}} \mathbf{u}^h\right)_Q - \left(\nabla \cdot \mathrm{w}^h, p^h\right)_Q$$
$$+ \left(\nabla \mathbf{w}^h, \nu \nabla \mathbf{u}^h\right)_Q + \left(q^h, \nabla \cdot \mathbf{u}^h\right)_Q - \left(\mathbf{w}^h, u_{\mathrm{n}}^{-h} \mathbf{u}^h\right)_{P_{\mathrm{ext}}^N} - \left(\mathbf{w}^h, \mathbf{f}\right)_Q, \tag{7c}$$

$$B_{\mathrm{VMS}}\left(\boldsymbol{U}^h, \boldsymbol{W}^h\right) = -\left(\nabla_{\hat{\mathbf{x}}} \mathbf{w}^h, \mathrm{u}' \otimes \hat{\mathbf{u}}^h\right)_{\bar{Q}} - \left(\nabla \mathbf{w}^h, \mathbf{u}^h \otimes \mathrm{u}'\right)_{\bar{Q}}$$
$$- \left(\nabla \mathbf{w}^h, \mathrm{u}' \otimes \mathrm{u}'\right)_{\bar{Q}} - \left(\nabla q^h, \mathrm{u}'\right)_{\bar{Q}} - \left(\nabla \cdot \mathrm{w}^h, p'\right)_{\bar{Q}}, \tag{7d}$$

$$B_{\mathrm{WBC}}\left(\boldsymbol{U}^h, \boldsymbol{W}^h\right) = \left(\mathbf{w}^h, p^h \mathbf{n} - \nu \nabla \mathbf{u}^h \cdot \mathbf{n}\right)_{P_{\mathrm{int}}} + \left(\nu \nabla \mathbf{w}^h \cdot \mathbf{n} - q^h \mathbf{n}, \mathbf{u}^h - \mathbf{u}_{\mathrm{int}}^D\right)_{P_{\mathrm{int}}}$$
$$+ \left(\mathbf{w}^h \tau_b, \mathbf{u}^h - \mathbf{u}_{\mathrm{int}}^D\right)_{P_{\mathrm{int}}}, \tag{7e}$$

$$B_{\mathrm{DC}}\left(\boldsymbol{U}^h, \boldsymbol{W}^h\right) = \left(\nabla \mathbf{w}^h, \nu_{dc} \nabla \mathbf{u}^h\right)_Q. \tag{7f}$$

Note: we have adopted the standard notation for the L_2 innerproduct, that is $(\boldsymbol{f}, \boldsymbol{g})_D = \int_D \boldsymbol{f} \cdot \boldsymbol{g} \, \mathrm{d}D$.

In (7d) the small-scale velocities $\mathbf{u}'$ and the small-scale pressure p' are modelled as

$$\mathbf{u}' = -\tau_M \mathbf{r}_M, \tag{8a}$$

$$p' = -\tau_C r_C, \tag{8b}$$

were τ_M and τ_C are stability parameters and $\mathbf{r}_M$ and r_C are the strong form residuals defined as

$$\mathbf{r}_M = \left(\hat{\mathbf{u}}^h \cdot \nabla_{\hat{\mathbf{x}}}\right) \mathbf{u}^h - \nabla p - \nu \nabla^2 \mathbf{u}^h - \mathbf{f}, \tag{9a}$$

$$r_C = \nabla \cdot \mathbf{u}^h. \tag{9b}$$

The small-scale contributions directly depend on the strong residuals, ensuring their consistency. For the stabilization parameters we use

$$\tau_M = \left(\hat{\mathbf{u}}^h \cdot \hat{\mathbf{G}} \hat{\mathbf{u}}^h + C_I \nu^2 \mathbf{G} : \mathbf{G}\right)^{-1/2}, \tag{10a}$$

$$\tau_C = \tau_M^{-1} \mathrm{Tr}\left(\mathbf{G}\right)^{-1}, \tag{10b}$$

where C_I is a user-provided input related to the inverse estimate, while $\hat{\mathbf{G}}$ and $\mathbf{G}$ are two metric tensors providing size and deformation information of the current element. The space–time metric tensor $\hat{\mathbf{G}}$ and the spatial metric tensor $\mathbf{G}$ are defined as

$$\hat{\mathbf{G}} = \left(\frac{\partial \xi}{\partial \hat{\mathbf{x}}}\right)^T \mathbf{G}_s \frac{\partial \xi}{\partial \hat{\mathbf{x}}}, \qquad \mathbf{G} = \left(\frac{\partial \xi}{\partial \mathbf{x}}\right)^T \frac{\partial \xi}{\partial \mathbf{x}}, \quad \text{with} \qquad \mathbf{G}_s = \begin{bmatrix} \mathbf{I}_{d\times d} & 0_{1\times d} \\ 0_{d\times 1} & s^2 \end{bmatrix}. \tag{11}$$

The terms in (7e) result from the weak enforcement of the Dirichlet boundary condition. They consist of a consistency term, a dual consistency term and a penalty term. For the penalty parameter, we use

$$\tau_b = \frac{1}{2} C_b \nu \left(\mathbf{n} \cdot \mathbf{G} \mathbf{n}\right)^{\frac{1}{2}}, \tag{12}$$

where C_b is a user-provided input related to a trace inequality.

The discontinuity capturing provided in (7e) results in additional diffusion in problem areas. The discontinuity capturing viscosity is inspired on [37],

$$\nu_{\mathrm{dc}} = 2 \frac{C_{\mathrm{dc}}}{\mathrm{Tr}\left(\mathbf{G}\right)^{1/2}} \frac{\|\mathbf{r}_M\|_2}{\|\nabla \mathbf{u}^h\|_F}, \tag{13}$$

where $\|\cdot\|_F$ denotes the Frobenius norm, and C_{dc} is a user defined coefficient. This type of discontinuity capturing viscosities is ubiquitous in the literature. Note that a VMS-based justification for this form of discontinuity capturing is given in [38,39]. Similar to the stabilization terms the additional viscosity scales with the size of the residual, this makes it a consistent term. This ensures the accuracy of the final solution.

These semi-linear forms in (7) are implemented using the MFEM library [40].

2.3. System of nonlinear ordinary differential equations

The formulation provided in (7) results in a non-linear system of algebraic equations. To aid the exposition of the reduced-order model in Section 2.4, we will explicitly provide this system here. We discretize the coarse scale variables with

$$u_1^h(\hat{\mathbf{x}}) = \boldsymbol{\phi}_{u_1} \cdot \mathbf{N}(\hat{\mathbf{x}}), \tag{14a}$$

$$u_2^h(\hat{\mathbf{x}}) = \boldsymbol{\phi}_{u_1} \cdot \mathbf{N}(\hat{\mathbf{x}}), \tag{14b}$$

$$p^h(\hat{\mathbf{x}}) = \boldsymbol{\phi}_{p} \cdot \mathbf{N}(\hat{\mathbf{x}}), \tag{14c}$$

where $\mathbf{N}(\hat{\mathbf{x}})$ is the array of shape functions, and $\boldsymbol{\phi}_{u_1}$, $\boldsymbol{\phi}_{u_2}$ and $\boldsymbol{\phi}_p$ are the arrays with unknown coefficients of the entire space–time domain. Note that $N(\hat{\mathbf{x}})$ does not need to be split into spatial and temporal components, as space and time are treated the same in the continuous space–time discretization.

The bilinear form in (7) becomes of the form

$$B\left(\boldsymbol{U}^h, \{\mathbf{N}, 0, 0\}\right) = \mathbf{b}_u + \mathbf{A}_{u_1u_1}\boldsymbol{\phi}_{u_1} + \mathbf{A}_{u_1u_2}\boldsymbol{\phi}_{u_2} + \mathbf{A}_{u_1p}\boldsymbol{\phi}_p + \mathbf{h}_{u_1}(\boldsymbol{\phi}_{u_1}, \boldsymbol{\phi}_{u_2}, \boldsymbol{\phi}_p), \tag{15a}$$

$$B\left(\boldsymbol{U}^h, \{0, \mathbf{N}, 0\}\right) = \mathbf{b}_{u_2} + \mathbf{A}_{u_2u_1}\boldsymbol{\phi}_{u_1} + \mathbf{A}_{u_2u_2}\boldsymbol{\phi}_{u_2} + \mathbf{A}_{u_2p}\boldsymbol{\phi}_p + \mathbf{h}_{u_2}(\boldsymbol{\phi}_{u_1}, \boldsymbol{\phi}_{u_2}, \boldsymbol{\phi}_p), \tag{15b}$$

$$B\left(\boldsymbol{U}^h, \{0, 0, \mathbf{N}\}\right) = \mathbf{b}_p + \mathbf{A}_{pu_1}\boldsymbol{\phi}_{u_1} + \mathbf{A}_{pu_2}\boldsymbol{\phi}_{u_2} + \mathbf{A}_{pp}\boldsymbol{\phi}_p + \mathbf{h}_p(\boldsymbol{\phi}_{u_1}, \boldsymbol{\phi}_{u_2}, \boldsymbol{\phi}_p), \tag{15c}$$

where $\mathbf{b}_x$ are the zeroth order terms, $\mathbf{A}_{xy}$ are the gradients defining the first order terms and $\mathbf{h}_x(\boldsymbol{\phi}_{u_1}, \boldsymbol{\phi}_{u_2}, \boldsymbol{\phi}_p)$ are the remaining higher order terms. In matrix–vector form this becomes

$$\begin{bmatrix} \mathbf{A}_{u_1u_1} & \mathbf{A}_{u_1u_2} & \mathbf{A}_{u_1p} \\ \mathbf{A}_{u_2u_1} & \mathbf{A}_{u_2u_2} & \mathbf{A}_{u_2p} \\ \mathbf{A}_{pu_1} & \mathbf{A}_{pu_2} & \mathbf{A}_{pp} \end{bmatrix} \begin{bmatrix} \boldsymbol{\phi}_{u_1} \\ \boldsymbol{\phi}_{u_2} \\ \boldsymbol{\phi}_p \end{bmatrix} + \begin{bmatrix} \mathbf{h}_{u_1}(\boldsymbol{\phi}_{u_1}, \boldsymbol{\phi}_{u_2}, \boldsymbol{\phi}_p) \\ \mathbf{h}_{u_2}(\boldsymbol{\phi}_{u_1}, \boldsymbol{\phi}_{u_2}, \boldsymbol{\phi}_p) \\ \mathbf{h}_p(\boldsymbol{\phi}_{u_1}, \boldsymbol{\phi}_{u_2}, \boldsymbol{\phi}_p) \end{bmatrix} = - \begin{bmatrix} \mathbf{b}_{u_1} \\ \mathbf{b}_{u_2} \\ \mathbf{b}_p \end{bmatrix}. \tag{16}$$

For added robustness, we solve the nonlinear algebraic equations using a pseudo-time globalization technique. The pseudo-time is denoted by θ. In the discrete weak formulation in (7), both the momentum and continuity equation are augmented with a pseudo-time rate term. For dimensional consistency, we scale the rate term in the continuity equation appropriately. The parameter a can be interpreted as an artificial speed of sound, parametrizing pseudo-compressibility [41–43]. Note, this is with respect to pseudo-time. The actual time derivative in (4) is unaffected and consistency of the formulation is maintained. The discrete problem in becomes:

Given $\boldsymbol{U}^n = \{\mathbf{u}^n, p^n\} \in \mathcal{W}^h$ *find* $\boldsymbol{U}^{n+1} = \left\{\mathbf{u}^{n+1}, p^{n+1}\right\} \in \mathcal{W}^h$ *such that for all* $\boldsymbol{W} = \left\{\mathbf{w}^h, q^h\right\} \in \mathcal{W}^h$*:*

$$B\left(\boldsymbol{U}(\boldsymbol{U}^n, \boldsymbol{U}^{n+1}), \boldsymbol{W}^h\right) + B_{\mathrm{PT}}\left(\partial_\theta \boldsymbol{U}(\boldsymbol{U}^n, \boldsymbol{U}^{n+1}), \boldsymbol{W}^h\right) = 0, \tag{17a}$$

where

$$B_{\mathrm{PT}}\left(\partial_\theta \boldsymbol{U}^h, \boldsymbol{W}^h\right) = \left(\mathbf{w}^h, \partial_\theta \mathbf{u}^h\right)_Q + \frac{1}{a^2}\left(q^h, \partial_\theta p^h\right)_Q. \tag{17b}$$

Additional interpolation rules for $\boldsymbol{U}\left(\boldsymbol{U}^n, \boldsymbol{U}^{n+1}\right)$ and $\partial_\theta \boldsymbol{U}\left(\boldsymbol{U}^n, \boldsymbol{U}^{n+1}\right)$ have to be specified to close the system. In this case, we select the backward Euler method, resulting in

$$\boldsymbol{U}\left(\boldsymbol{U}^n, \boldsymbol{U}^{n+1}\right) = \boldsymbol{U}^{n+1}, \tag{18a}$$

$$\partial_\theta \boldsymbol{U}\left(\boldsymbol{U}^n, \boldsymbol{U}^{n+1}\right) = \frac{1}{\Delta\theta}(\boldsymbol{U}^{n+1} - \boldsymbol{U}^n), \tag{18b}$$

where $\Delta\theta$ is a user-specified pseudo-time step size.

Using the mass matrix,

$$\mathbf{M} = \int_Q \mathbf{N} \otimes \mathbf{N} dQ, \tag{19}$$

and dropping the superscript gives the following non-linear system of algebraic equations:

$$\begin{aligned} &\left(\frac{1}{\Delta\theta}\begin{bmatrix} \mathbf{M}_{u_1} & 0 & 0 \\ 0 & \mathbf{M}_{u_2} & 0 \\ 0 & 0 & \frac{1}{a^2}\mathbf{M}_p \end{bmatrix} + \begin{bmatrix} \mathbf{A}_{u_1u_1} & \mathbf{A}_{u_1u_2} & \mathbf{A}_{u_1p} \\ \mathbf{A}_{u_2u_1} & \mathbf{A}_{u_2u_2} & \mathbf{A}_{u_2p} \\ \mathbf{A}_{pu_1} & \mathbf{A}_{pu_2} & \mathbf{A}_{pp} \end{bmatrix}\right)\begin{bmatrix} \boldsymbol{\phi}_u \\ \boldsymbol{\phi}_v \\ \boldsymbol{\phi}_p \end{bmatrix} \\ &\qquad + \begin{bmatrix} \mathbf{h}_{u_1}(\boldsymbol{\phi}_{u_1}, \boldsymbol{\phi}_{u_2}, \boldsymbol{\phi}_p) \\ \mathbf{h}_{u_2}(\boldsymbol{\phi}_{u_1}, \boldsymbol{\phi}_{u_2}, \boldsymbol{\phi}_p) \\ \mathbf{h}_p(\boldsymbol{\phi}_{u_1}, \boldsymbol{\phi}_{u_2}, \boldsymbol{\phi}_p) \end{bmatrix} = - \begin{bmatrix} \mathbf{b}_{u_1} \\ \mathbf{b}_{u_2} \\ \mathbf{b}_p \end{bmatrix} + \frac{1}{\Delta\theta}\begin{bmatrix} \mathbf{M}_{u_1}\boldsymbol{\phi}_{u_1}^n \\ \mathbf{M}_{u_2}\boldsymbol{\phi}_{u_2}^n \\ \frac{1}{a^2}\mathbf{M}_p\boldsymbol{\phi}_p^n \end{bmatrix} \end{aligned} \tag{20}$$

Note that the time-dependent contributions are incorporated in the matrices $\mathbf{A}_{xy}$ and vectors $\mathbf{h}_x$, while the pseudo-time contributions are represented by the first and last terms respectively. This problem is solved using a modified Newton iteration method, while the parallel sparse matrix problems are solved using precondition and GMRES provided by the Hypre library [44].

2.4. Reduced basis using Proper-Orthogonal Decomposition

The dimensionality n_f of the system of the full-order model in (20) is inherently large. This imposes a large computational effort. For scenarios involving solving numerous closely related problems, such as parameter studies or design optimization, there is an opportunity to mitigate this computational burden. We can reuse previously obtained solutions, leading to a remarkable reduction in computational effort with only a minor reduction in solution fidelity.

We find the reduced-order model basis $\mathbf{V}$ using a discrete Proper Orthogonal Decomposition (POD) [45]. The POD generates a low-dimensional basis by finding meaningful behaviour in low-dimensional patterns of dynamic activity tailored to particular dynamics and parameters. The discrete POD consists of a singular value decomposition of a snapshot matrix $\mathbf{X}$ containing m full-order solutions in its columns. The full-order solutions are determined using a particular set of input parameters μ, which is a sample from a larger parameter space Θ. Each entry of the snapshot matrix contains one entire space–time solution of a full-order solution for a parameter set μ. The singular value decomposition is given as

$$\mathbf{X} = \Phi \mathbf{\Sigma} \Psi^T, \tag{21}$$

where Φ contains the POD modes in the left singular vectors, Ψ gives the right singular vectors and $\mathbf{\Sigma}$ gives the singular values in the diagonal. The expansion coefficients of the ROM basis have standard algebraic orthogonality such that $\mathbf{V}^T\mathbf{V} = \boldsymbol{I}$. The singular values are ordered from smallest to largest with $\sigma_i < \sigma_{i+1} < \sigma_m$, indicating the relevance of the corresponding modes. We find the basis $\mathbf{V}$ by choosing it as the first n_r columns of Φ based on a fraction of the missing energy in the basis

$$\epsilon_{\text{POD}} = \frac{\sum_i^{n_r} \sigma_i}{\sum_i^{m} \sigma_i}. \tag{22}$$

2.5. Projection-based reduced-order model

We reduce each variable separately and reduce the dimension of the system by restricting each variable to its own subspace. The reduced system approximates the entire space–time solution of the original system in a subspace spanned by a solution basis

$$\boldsymbol{\phi}_{u_1} \approx \tilde{\boldsymbol{\phi}}_{u_1} = \mathbf{V}_{u_1} \hat{\boldsymbol{\phi}}_{u_1}, \tag{23a}$$

$$\boldsymbol{\phi}_{u_2} \approx \tilde{\boldsymbol{\phi}}_{u_2} = \mathbf{V}_{u_2} \hat{\boldsymbol{\phi}}_{u_2}, \tag{23b}$$

$$\boldsymbol{\phi}_{p} \approx \tilde{\boldsymbol{\phi}}_{p} = \mathbf{V}_{p} \hat{\boldsymbol{\phi}}_{p}. \tag{23c}$$

Here, $\boldsymbol{\phi}_x$ is the sought for full-order solution, while $\tilde{\boldsymbol{\phi}}_x$ is its the high-dimensional representation of the reduced-order model approximation ($\text{size}(\tilde{\boldsymbol{\phi}}_x) = n_f$). Contrary $\hat{\boldsymbol{\phi}}_x$ is the low dimensional representation and $\mathbf{V}_x$ is the reduced basis as found in the previous section ($\text{size}(\hat{\boldsymbol{\phi}}_x) = n_r$). The matrix $\mathbf{V}_x$ serves as a linear map between the low-dimensional and high-dimensional representation of the reduced-order solution The basis $\mathbf{V}_x$ is composed of n_{rx} space–time basis vectors $\boldsymbol{v}_x$ as columns, $\mathbf{V}_x = \left\{ \boldsymbol{v}_{x1}, ..., \boldsymbol{v}_{xn_{rx}} \right\}$ with $n_r \ll n_f$.

As the reduced-order model will be a direct projection of the full-order model, it implicitly uses the same stabilization as the full-order model. This is akin to work on POD-Galerkin reduced-order models with the variational multi-scale frame-work [10,26,29]. Upon substitution of (23) in (16), the number of unknowns reduces while the number of equations remains the same, resulting in an over-determined system. We apply a Galerkin projection to find the reduced system of equations. This is equivalent to using the subspace restriction of the trial-space on the test spaces as well.

In this case the full-order model (16) is reduced to

$$\begin{bmatrix} \mathbf{V}_{u_1} \\ \mathbf{V}_{u_2} \\ \mathbf{V}_{p} \end{bmatrix}^T \begin{bmatrix} \mathbf{A}_{u_1u_1} & \mathbf{A}_{u_1u_2} & \mathbf{A}_{u_1p} \\ \mathbf{A}_{u_2u_1} & \mathbf{A}_{u_2u_2} & \mathbf{A}_{u_2p} \\ \mathbf{A}_{pu_1} & \mathbf{A}_{pu_2} & \mathbf{A}_{pp} \end{bmatrix} \begin{bmatrix} \mathbf{V}_{u_1} \boldsymbol{\phi}_{u_1} \\ \mathbf{V}_{u_2} \boldsymbol{\phi}_{u_2} \\ \mathbf{V}_{p} \boldsymbol{\phi}_{p} \end{bmatrix} + \begin{bmatrix} \mathbf{V}_{u_1} \\ \mathbf{V}_{u_2} \\ \mathbf{V}_{p} \end{bmatrix}^T \begin{bmatrix} \mathbf{h}_{u_1}(\mathbf{V}_{u_1} \boldsymbol{\phi}_{u_1}, \mathbf{V}_{u_2} \boldsymbol{\phi}_{u_2}, \mathbf{V}_{p} \boldsymbol{\phi}_{p}) \\ \mathbf{h}_{u_2}(\mathbf{V}_{u_1} \boldsymbol{\phi}_{u_1}, \mathbf{V}_{u_2} \boldsymbol{\phi}_{u_2}, \mathbf{V}_{p} \boldsymbol{\phi}_{p}) \\ \mathbf{h}_{p}(\mathbf{V}_{u_1} \boldsymbol{\phi}_{u_1}, \mathbf{V}_{u_2} \boldsymbol{\phi}_{u_2}, \mathbf{V}_{p} \boldsymbol{\phi}_{p}) \end{bmatrix} = - \begin{bmatrix} \mathbf{V}_{u_1} \\ \mathbf{V}_{u_2} \\ \mathbf{V}_{p} \end{bmatrix}^T \begin{bmatrix} \mathbf{b}_{u_1} \\ \mathbf{b}_{u_2} \\ \mathbf{b}_{p} \end{bmatrix},$$

which can be alternatively written as

$$\begin{bmatrix} \hat{\mathbf{A}}_{u_1u_1} & \hat{\mathbf{A}}_{u_1u_2} & \hat{\mathbf{A}}_{u_1p} \\ \hat{\mathbf{A}}_{u_2u_1} & \hat{\mathbf{A}}_{u_2u_2} & \hat{\mathbf{A}}_{u_2p} \\ \hat{\mathbf{A}}_{pu_1} & \hat{\mathbf{A}}_{pu_2} & \hat{\mathbf{A}}_{pp} \end{bmatrix} \begin{bmatrix} \hat{\boldsymbol{\phi}}_{u_1} \\ \hat{\boldsymbol{\phi}}_{u_2} \\ \hat{\boldsymbol{\phi}}_{p} \end{bmatrix} + \begin{bmatrix} \hat{\mathbf{h}}_{u_1}(\mathbf{V}_{u_1} \hat{\boldsymbol{\phi}}_{u_1}, \mathbf{V}_{u_2} \hat{\boldsymbol{\phi}}_{u_2}, \mathbf{V}_{p} \hat{\boldsymbol{\phi}}_{p}) \\ \hat{\mathbf{h}}_{u_2}(\mathbf{V}_{u_1} \hat{\boldsymbol{\phi}}_{u_1}, \mathbf{V}_{u_2} \hat{\boldsymbol{\phi}}_{u_2}, \mathbf{V}_{p} \hat{\boldsymbol{\phi}}_{p}) \\ \hat{\mathbf{h}}_{p}(\mathbf{V}_{u_1} \hat{\boldsymbol{\phi}}_{u_1}, \mathbf{V}_{u_2} \hat{\boldsymbol{\phi}}_{u_2}, \mathbf{V}_{p} \hat{\boldsymbol{\phi}}_{p}) \end{bmatrix} = - \begin{bmatrix} \hat{\mathbf{b}}_{u_1} \\ \hat{\mathbf{b}}_{u_2} \\ \hat{\mathbf{b}}_{p} \end{bmatrix}, \tag{24}$$

where

$$\hat{\mathbf{A}}_{xy} = \mathbf{V}_x^T \mathbf{A}_{xy} \mathbf{V}_y, \tag{25a}$$

$$\hat{\mathbf{h}}_{x}(\cdot) = \mathbf{V}_x^T \mathbf{h}_{x}(\cdot), \tag{25b}$$

$$\hat{\mathbf{b}}_{x} = \mathbf{V}_x^T \mathbf{b}_{x}. \tag{25c}$$

Note that $\hat{\mathbf{A}}_{xy}$ can be precomputed if it is independent of parameter μ. Additionally, it is worth noting that we do not use pseudo-time as a globalization technique in the reduced-order model. The non-linearity did not pose issues in solving the problem. The reduced-order model is unable to represent arbitrary unphysical flow features as it is constrained by the basis. We conjecture that this is the reason that a globalization technique such as pseudo-time is not needed in the reduced-order mode. Our experience showed that it was not necessary.

For obtaining the POD basis and implementing the reduced-order model we use the libROM library [46].

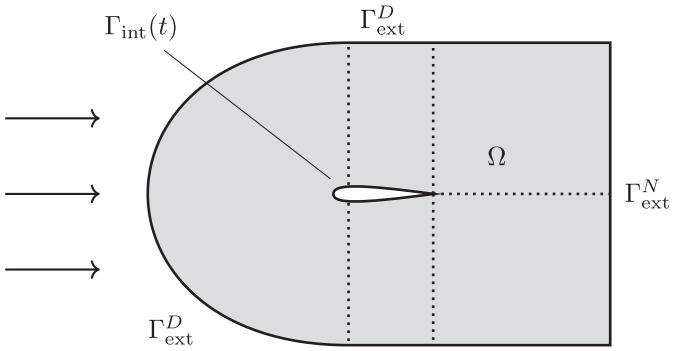

Fig. 2. Schematic representation of the domain Ω, as an iso-time slice of P, surrounding the hydrofoil with the no-slip boundary Γ_{int}, the inflow boundary Γ^D_{ext} and the outflow boundary Γ^N_{ext}. The arrows indicate the direction of the flow. The five NURBS patches are indicated with a dotted line.

3. Numerical experiments

In this section, we apply the presented reduced-order model to simulate the flow past a periodically moving two-dimensional hydrofoil. First, we discuss the general setup of the problem, its discretization and numerical parameters. Following the general setup, we provide an overview of the reduced-order model's specifics and explain the metrics used for evaluation. After these preliminaries, we conduct three parameter studies, systematically varying parameters such as period, viscosity, and motion profile. This will provide a clear demonstration of the potential offered by the reduced-order model.

3.1. Problem setup

A typical isotime slice of the computational domain is given in Fig. 2. The hydrofoil has a NACA 0012 profile with a chord denoted as c. To find a reasonable balance between artificial boundary influences and computational effort, the size of the domain is chosen to be 8 chords in the upwind and lateral directions and 8 chords in the downwind direction. The inflow from the left is a uniform flow, this velocity is denoted as U. The foil experiences a forced heave motion, with amplitude h_a.

In the first two experiments, the motion is sinusoidal and given by

$$h(t) = h_a \sin\left(\frac{2\pi t}{T}\right), \tag{26}$$

where T is the period. To correctly categorize the motion, we introduce the Strouhal number

$$\text{St} = \frac{2\ h_a}{U\ T}. \tag{27}$$

Furthermore, we will use the chord Reynolds number and force coefficients to non-dimensionalize the system,

$$\text{Re} = \frac{U\ c}{\nu}, \qquad C_x = \frac{F_x}{\frac{1}{2}\ \rho U^2 c}. \tag{28}$$

3.1.1. Discretization

The full-order model formulation in (7) is evaluated using isogeometric analysis. We discretize the domain using five second-order NURBS patches. This results in C^1-continuity within each patch and C^0-continuity over patch interfaces. The boundaries of the NURBS patches are indicated with the dotted lines in Fig. 2. The patches are extruded in the time direction, resulting in 3D NURBS patches. We satisfy the time-periodic boundary condition with C^0-continuous constraints.

The motion of the foil section is accommodated by appropriately shaping the space–time mesh a priori. This is achieved by first applying knot insertion to fit the shape of Γ_{int} to be the foil section on each time slab of P_{int}. Then, knots are inserted in the time direction to apply the prescribed motion on P_{int}. The resulting mesh contains the entire discretized space–time domain of the time-periodic problem. The boundaries of the resulting discretized domain are shown in Fig. 3. Here, one of the time-periodic boundaries is cut off, revealing the shape of P_{int}, which governs the motion of $\Gamma_{\text{int}}(t)$. We refer to [50] for knot insertion and fitting algorithms.

This discretization results in 900k degrees-of-freedom per variable, making a total system size of 2.7M degrees-of-freedom. We use 49 control points in the time direction. See Appendix A for details regarding the discretization choice and time slices of the mesh. Further refinement of the discretization gives only a small improvement of the solution and does not compensate for the additional computational costs.

3.1.2. Numerical parameters

Due to the non-dimensional nature of the problem, the choice for freestream and chord is largely immaterial. For simplicity, we choose unity, that is $U = 1$ and $c = 1$. The time-dependent boundary velocities $\mathbf{u}^D_{\text{int}}(t)$ on the internal boundary are governed by the

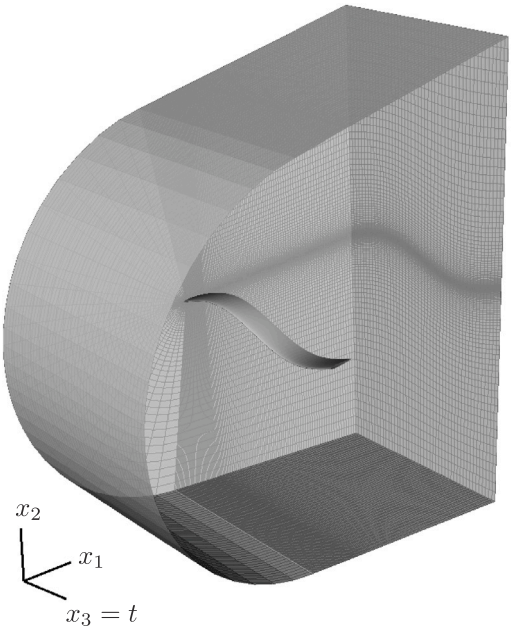

Fig. 3. The boundaries of the resulting discretized domain. The shape of P_{int}, which governs the motion of $\Gamma_{\text{int}}(t)$, is revealed as one of the time-periodic boundaries is cut off. See Appendix A for time slices of the mesh.

Table 1
Numerical parameters and their corresponding values.

Parameter	Value
s	1
a	4
C_I	36
C_b	8
C_{dc}	0.3
$\Delta\theta$	1.0

space–time mesh and are not given as an input. The velocity $\mathbf{u}_{\text{int}}^D$ is computed with the derivative of the spatial coordinate $\mathbf{x}$ to the time direction $t = x_{d+1}/s$

$$\mathbf{g}_{\text{int}} = \left.\frac{\partial \mathbf{x}}{\partial t}\right|_{\mathbf{x}_{\text{p}}} \quad \text{in} \quad P_{\text{int}}, \tag{29}$$

where $\mathbf{x}_{\text{p}}$ is a particle path on the solid of P_{int}. See [9] for more details. Other relevant numerical parameters are given in Table 1.

For the convergence criterion, we choose an absolute tolerance of 10^{-5} for the two momentum conservation and mass conservation residuals of both the full-order and reduced-order model. For the full-order model, the residual is evaluated at the beginning of each pseudo-time step [9]. Tighter convergence criteria only result in negligible changes to the solution.

3.1.3. Reduced-order model

The reduced-order model as presented in (24) is constructed and evaluated in three stages: an offline, merge and online stage. In the offline stage, we evaluate the full-order model for 30 values of the input parameter μ, chosen with equal distance in the parameter space Θ. In the merge stage, the snapshot matrix of the time-periodic space–time solution of the full-order model is assembled and the solution basis $\mathbf{V}_x$ is computed using a POD. In the online stage, the system in (24) is constructed and solved.

We compute the forces of the full-order model similar to [9], using a space–time force extraction method inspired by the variationally consistent postprocessing method [47,48]. For clarity, we repeat it here. The time-dependent force is given by

$$\mathbf{F}(t) = \int_{\Gamma_{\text{int}}} p\mathbf{n} - \nu\nabla\mathbf{u}\cdot\mathbf{n} + \tau_b(\mathbf{u}-\mathbf{g})\mathrm{d}\Gamma \tag{30}$$

which requires a spatial integral at a fixed time level. For arbitrary space–time meshes evaluation of this integral is not trivial. We remedy this by discretizing the force in time,

$$\mathbf{F}^h(t) = \mathbf{F}_a N_a(t), \tag{31}$$

and project the signal as follows

$$\int_{\mathcal{I}} \mathbf{F}_a \; N_a N_b \; \mathrm{d}t = \int_{P_{\text{int}}} \left(p\mathbf{n} - \nu \nabla \mathbf{u} \cdot \mathbf{n} + \tau_b(\mathbf{u} - \mathbf{g})\right) \; N_b \; \mathrm{d}t, \tag{32}$$

which only involves integrals that are easily evaluated. Note that the last term on the right-hand side is the contribution of the weak boundary condition.

3.1.4. Performance metrics

We evaluate the accuracy of the reduced-order model by evaluating the normalized l_2-norm of the error for each variable. The error is the difference between the full-order solution, $\boldsymbol{\phi}_x$, and the full representation of the reduced-order solution, $\tilde{\boldsymbol{\phi}}_x$, over the entire space–time domain

$$\epsilon_x = \sqrt{(\tilde{\boldsymbol{\phi}}_x - \boldsymbol{\phi}_x) \cdot (\tilde{\boldsymbol{\phi}}_x - \boldsymbol{\phi}_x)} / \sqrt{\boldsymbol{\phi}_x \cdot \boldsymbol{\phi}_x}, \tag{33}$$

where x is a place holder for the different variables u_1, u_2 and p. The error is normalized with the l_2-norm of the full-order solution of the entire space–time domain. The speed-up of the reduced-order model (ROM) over the full-order model (FOM) is defined as

$$\text{speed-up} = \frac{\text{wall-clock time FOM}}{\text{wall-clock time ROM}}. \tag{34}$$

The wall-clock time only includes the solve time of the non-linear system and excludes the assembly of the matrix.

We evaluate the accuracy of the computed forces $\mathbf{F}$ using the average and root mean square error for each component. For a generic force component F we compute these as

$$\epsilon_{\text{avg}} = \frac{1}{T} \int_{\mathcal{I}} \tilde{\mathrm{F}}^h - \mathrm{F}^h \mathrm{d}t = \frac{1}{} \sum_{i=1} \tilde{\mathrm{F}}^h(t_i) - \mathrm{F}^h(t_i), \tag{35}$$

$$\epsilon^2_{\text{RMS}} = \frac{1}{T} \int_{\mathcal{I}} \left(\tilde{\mathrm{F}}^h - \mathrm{F}^h\right)^2 \mathrm{d}t = \frac{1}{} \sum_{i=1} \left(\tilde{\mathrm{F}}^h(t_i) - \mathrm{F}^h(t_i)\right)^2, \tag{36}$$

where is a specified number of samples and $t_i = \frac{i}{}T$. To get a more meaningful quantification of the error, the average and RMS errors are normalized with the range of the data ΔF,

$$\epsilon_{\text{navg}} = \frac{\epsilon_{\text{avg}}}{\Delta F}, \qquad \epsilon_{\text{nRMS}} = \frac{\epsilon_{\text{RMS}}}{\Delta F}, \tag{37}$$

where the range of the data is obtained using

$$\Delta F = \max_{i=1..} \left(\mathrm{F}^h(t_i)\right) - \min_{i=1..} \left(\mathrm{F}^h(t_i)\right). \tag{38}$$

3.2. Parameter studies

In this section, we evaluate three studies considering a variation in Strouhal number, Reynolds number and motion profile. For each scenario, we first discuss the general description of the problem and assess its reducibility, followed by a review of the results and the error metrics described earlier.

3.2.1. Strouhal number study

In this experiment, we will vary the Strouhal number and evaluate the efficacy of the reduced-order model to deal with this parameter change. The Strouhal number St is a measure of the velocity of the motion relative to the free-stream velocity. For flat objects with flapping motions, such as heaving foil sections, the range of $St = 0.1$ to $St = 0.3$ is of particular interest. Due to the interaction of the shed vortex with the foil section, it will make the transition from drag to thrust producing when St is increased in this range.

We will be looking at four different Strouhal numbers spread over the range of interest, that is

$$St \in [0.105, 0.155, 0.205, 0.255], \tag{39}$$

while we fix the motion amplitude $h_a/c = 0.5$. For the Reynolds number we set Re = 800. Two typical velocity fields computed by the reduced-order model and full-order model, for $St = 0.105$ and $St = 0.255$, are depicted in Fig. 4. The figure shows the agreement between the two velocity fields. Note that the wake interaction is qualitatively different. This qualitative difference is also reflected in the force signals as depicted in Figs. 8 and 9, particularly the force in the x_1 direction is notably different.

To speed up the computations, we build a reduced-order model for a sinusoidal heaving foil section with a variation in Strouhal number. In the offline stage, we compute 30 equidistant snapshots in the range $0.08 \leq \mathrm{St} \leq 0.28$. The Strouhal numbers we are interested in, given in (39), are not in this set. To extract an efficient basis for the reduced-order model out of the snapshots we compute the SVD of the snapshot matrix. The two most dominant modes of the basis of u_1, u_2 and p are visualized in Appendix B. The singular values σ_i of this decomposition are given in Fig. 5.

From the steep decline in σ_i it can be concluded that the problem is suitable for reduction. Using the singular values, the missing energy fraction ϵ_{POD} for different reduced bases can be computed. The required size of the reduced basis for a given missing energy fraction ϵ_{POD} is indicated in Table 2.

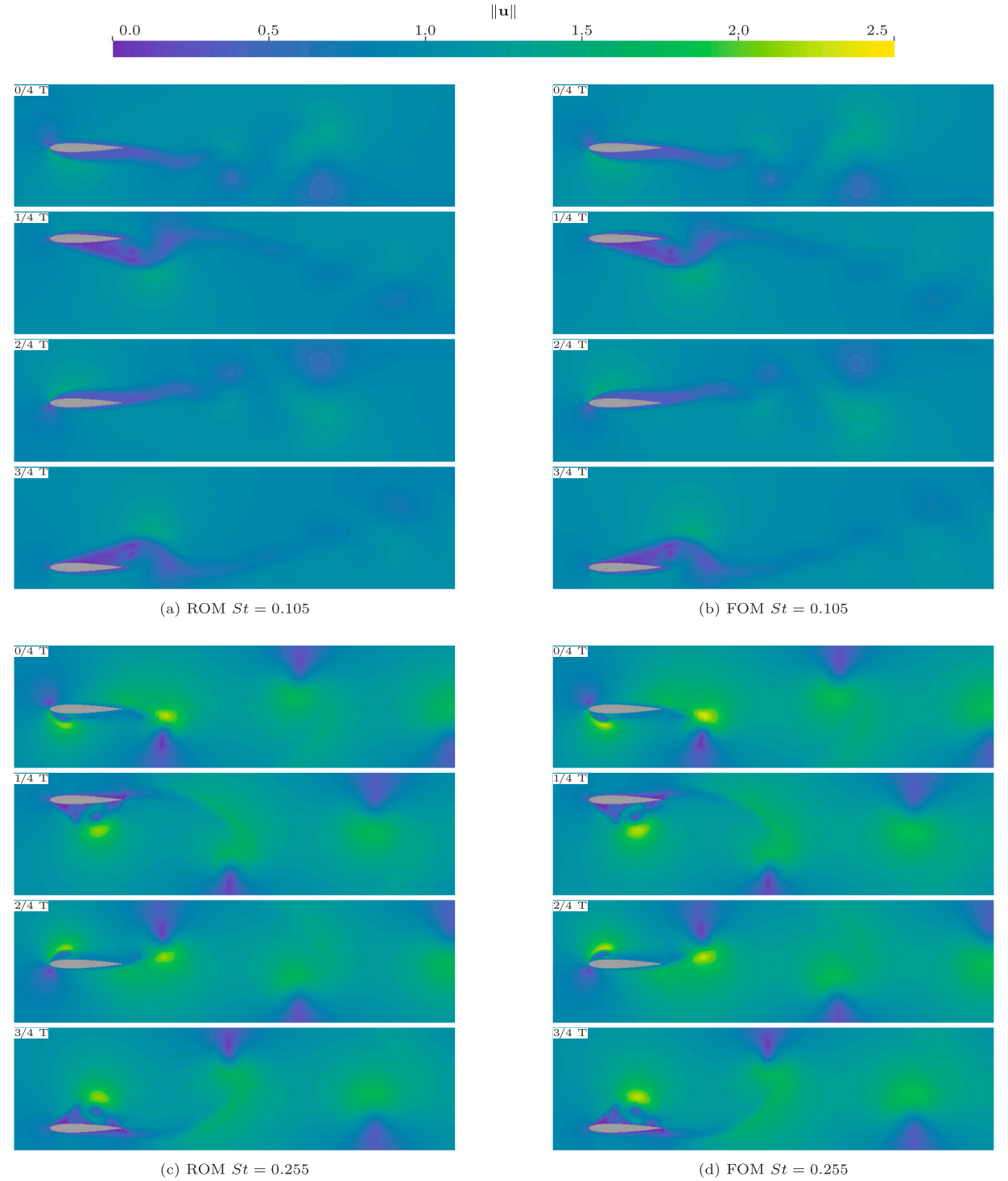

(a) ROM $St = 0.105$ (b) FOM $St = 0.105$

(c) ROM $St = 0.255$ (d) FOM $St = 0.255$

Fig. 4. Strouhal number study: Magnitude of the velocity $\|\mathbf{u}\|$ computed by the reduced-order model (ROM) and full-order model (FOM) at $t = 0$, $t = \frac{1}{4}T$, $t = \frac{2}{4}T$, $t = \frac{3}{4}T$ for $St = 0.105$ and $St = 0.255$. Visualized using VisIt [49].

For these five different reduced bases the speed-up and errors in solution and force are given in Fig. 6. The solution error is computed as $\epsilon = \sqrt{\epsilon_{u_1}^2 + \epsilon_{u_2}^2 + \epsilon_p^2}$, using (33). The force errors are given by (35) and (36) and are averaged over the four Strouhal numbers. As expected the figure shows that the errors decrease if the missing energy fraction ϵ_{POD} is decreased. The speed-up also

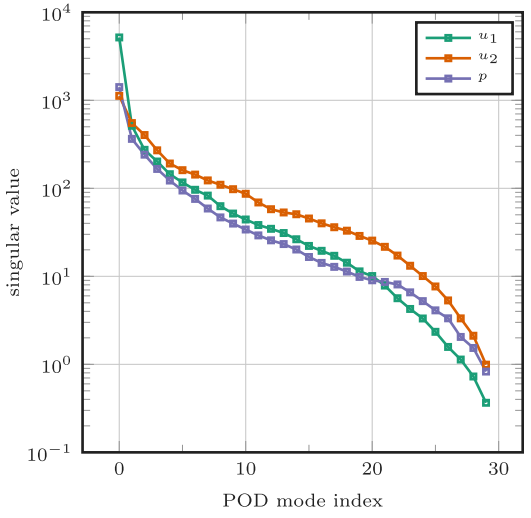

Fig. 5. Strouhal number study: Decay of singular values σ_i associated with $\mathbf{V}$.

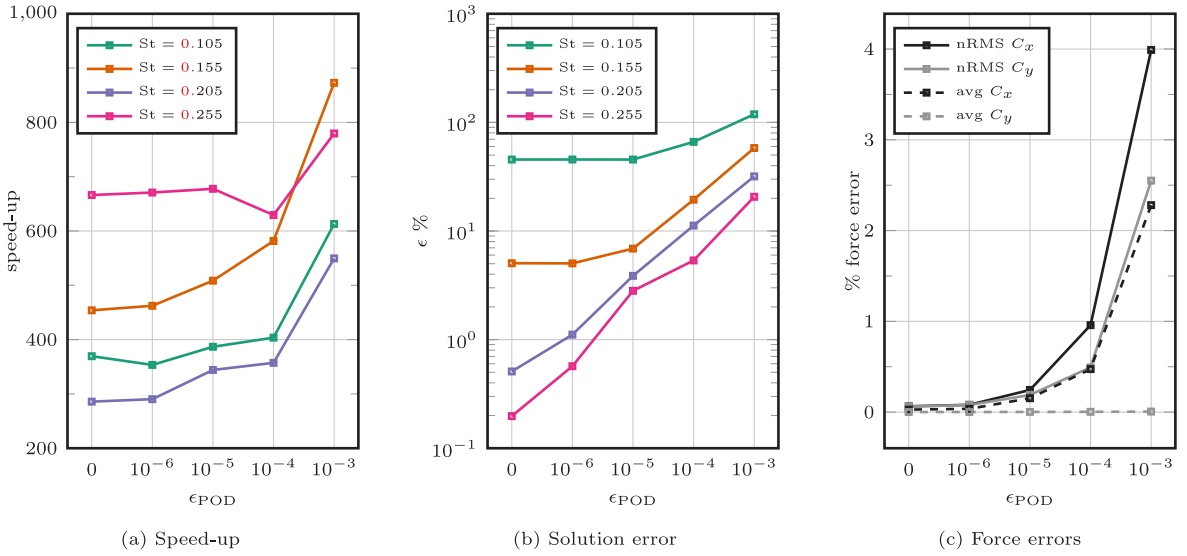

(a) Speed-up (b) Solution error (c) Force errors

Fig. 6. Strouhal number study: Reduced-order mode speed-up and convergence of the error as function of the missing energy fraction ϵ_{POD} as given in Table 2.

Table 2
Strouhal number study: Basis size n_r per variable per missing energy fraction ϵ_{POD} Eq. (22).

ϵ_{POD}	size u_1	size u_2	size p
10^{-3}	7	20	13
10^{-4}	14	25	22
10^{-5}	20	27	26
10^{-6}	24	29	29
0	30	30	30

decreases but is still significant. Note that the errors of the forces converge to zero. Below $\epsilon_{\text{POD}} < 10^{-4}$ the speed-up does not further deteriorate, therefor we choose $\epsilon_{\text{POD}} = 0$ for further experiments as this gives a favourable compromise between speed-up and errors.

For higher Strouhal numbers the errors are smaller as can be seen in Fig. 6. The contribution of the separate variables u_1, u_2, and p to these errors are given in Fig. 7. This is likely a consequence of the sampling of the parameter space used for generating the snapshots. Alternatively, instead of opting for a uniform sampling of the Strouhal number, one could have chosen a uniform sampling of the period T, or equivalently $1/St$, which would have resulted in a higher density of samples at low Strouhal numbers.

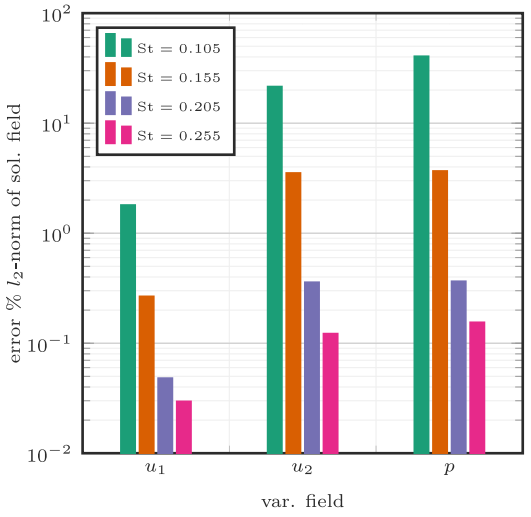

Fig. 7. Strouhal number study: normalized l_2-norm of the error ϵ_x (33) of reduced-order w.r.t. full-order model.

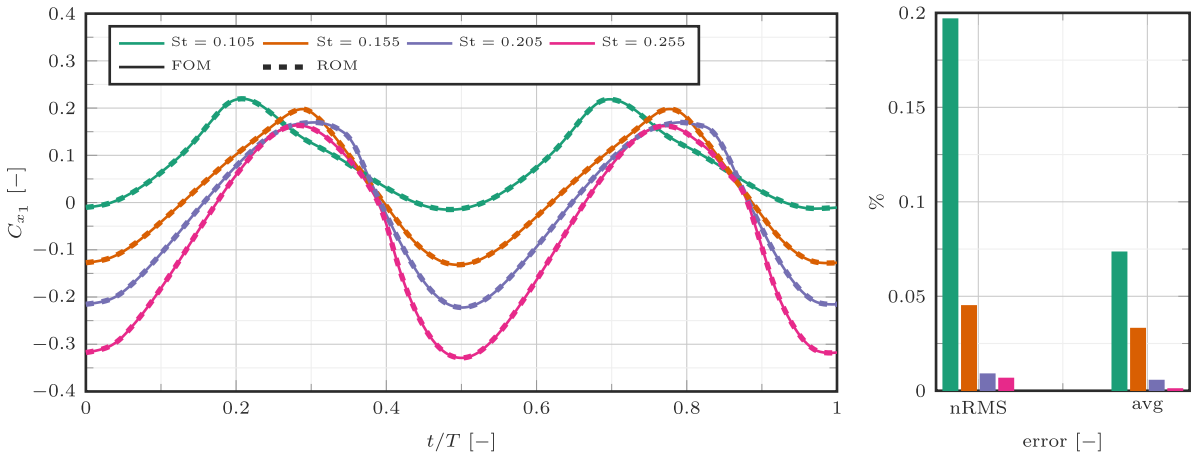

Fig. 8. Strouhal number study: Horizontal force coefficient C_{x_1} and corresponding normalized RMS error and absolute error of the average force for reduced-order w.r.t. full-order model.

Another implementation of this experiment, with a uniform sampling of the period T, indeed showed smaller errors at low Strouhal numbers. Note that choices considering the sampling density can be avoided with the employment of an adaptive sampling method, leading to more uniform errors in the parameter space. The error for u_1 is smaller than the errors for u_2 and p. This can be explained by the normalized nature of ϵ_v. The norm of u_1 is dictated by the free stream velocity U.

The computed forces of the reduced-order and full-order models are given in Figs. 8 and 9.

The corresponding normalized RMS (36) and average (35) error are also provided. The agreement between the forces is very good. For the forces in the x_1-direction and the x_2-direction the errors are <0.2%. Note that the full-order and reduced-order models use different force extraction methods.

3.2.2. Reynolds number study

The Reynolds number Re describes the ratio of inertial forces to viscous forces in fluid flow. It helps to characterize the flow regime, indicating whether it is laminar, transitional, or turbulent. We study low Reynolds number flow with $\mathrm{Re} < 10^3$, below the transition regime to turbulent flow. An increase in Reynolds number can be linked to either an increase in forward velocity or a decrease in viscosity. As the Reynolds number increases, we anticipate a reduction in drag forces and an increase in lift forces.

We create a reduced-order model for a sinusoidal heaving foil section with a variation in Reynolds number, $200 \leq \mathrm{Re} \leq 800$. We choose a constant Strouhal number of $St = 0.125$ and a constant motion amplitude $h_a/c = 0.5$. Fig. 10 shows a steep decrease of the singular values σ_i, indicating that the problem is reducible. We evaluate the reduced-order model, and the full-order model as ground truth, at

$$\mathrm{Re} \in [275, 425, 575, 725]. \tag{40}$$

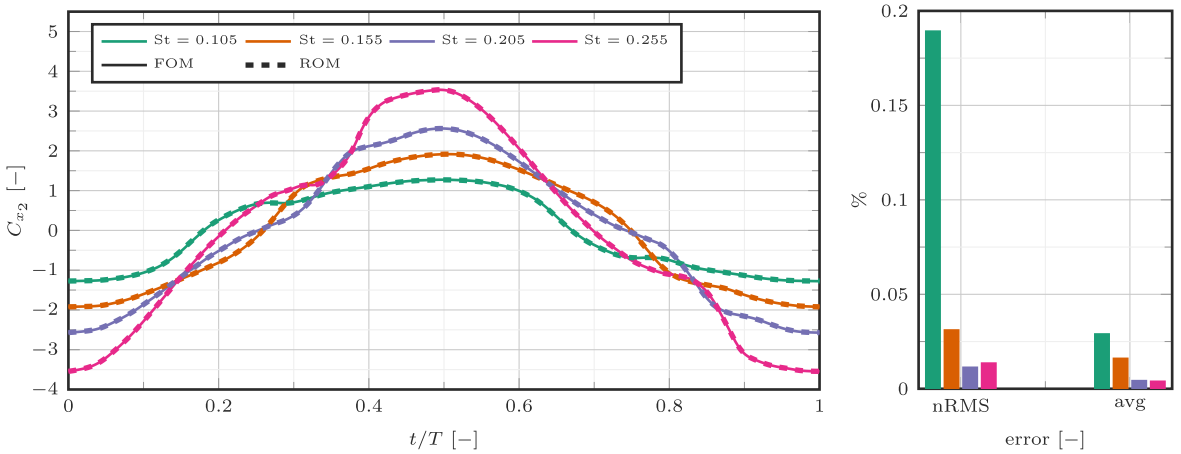

Fig. 9. Strouhal number study: Vertical force coefficient C_{x_2} and corresponding normalized RMS error and absolute error of the average force for reduced-order w.r.t. full-order model.

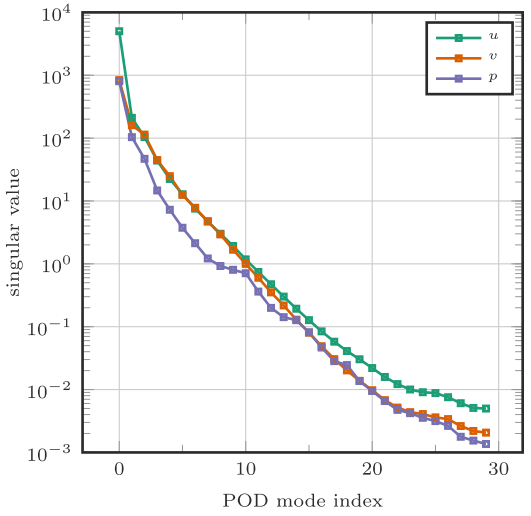

Fig. 10. Decay of singular values σ_i associated with $\mathbf{V}$ for the Reynolds number study.

These Reynolds numbers do not coincide with the Reynolds numbers used to generate the snapshots.

Fig. 11 gives the relative error (33) for the variable fields when comparing the reduced-order model with the full-order model. The errors are the smallest for the u_1-solution field. The errors for the p-solution field are the largest. All errors are $\leq \mathcal{O}(1\%)$.

Figs. 12 and 13 show the agreement between the computed forces of the full-order and reduced-order models. The normalized root mean square error (36) and the normalized error of the average (35) are <0.08% and <0.05% for C_{x_1} and C_{x_2} respectively.

3.2.3. Motion profile study

The motion profile significantly influences thrust production in a flapping wing. An optimized motion profile can enhance aerodynamic efficiency by maximizing lift and minimizing drag, ultimately leading to more effective thrust production. We study a group of non-sinusoidal motion profiles described with

$$h(t) = h_a \sin(\omega t + \phi(t),) \tag{41a}$$

$$\phi(t) = \phi_a \cos(\omega t). \tag{41b}$$

The time trace of this motion is given in Fig. 14.

The time-dependent phase-shift modulation $\phi(t)$ is time-periodic, resulting in a time-periodic heave. As ϕ_a increases, the original sinusoidal motion is distorted in an unsymmetric way. At a positive heave, the motion slows down, while at a negative heave, the motion speeds up. This results in an uneven dwell time in the upper and lower parts of the stroke.

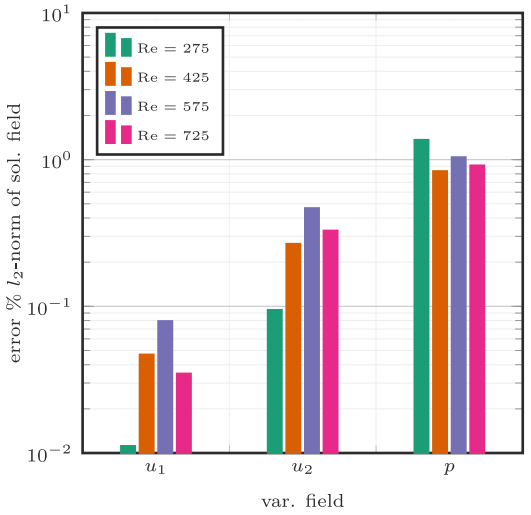

Fig. 11. l_2-norm of the error ϵ_x (33) of reduced-order w.r.t. full-order model normalized with the l_2-norm of the solution field for the Reynolds number study.

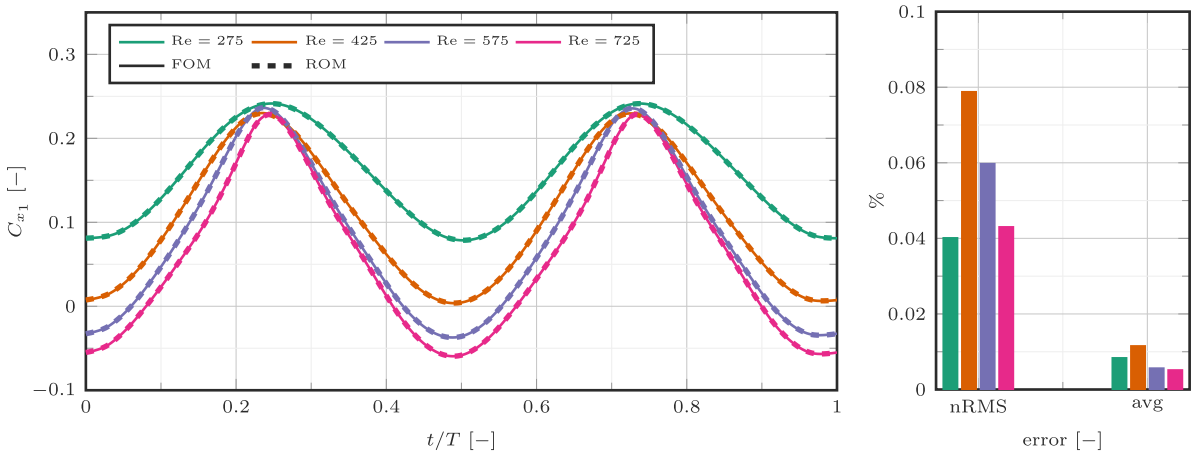

Fig. 12. Reynolds number study: Horizontal force coefficient C_{x_1} and corresponding normalized RMS error and absolute error of the average force for reduced-order w.r.t. full-order model.

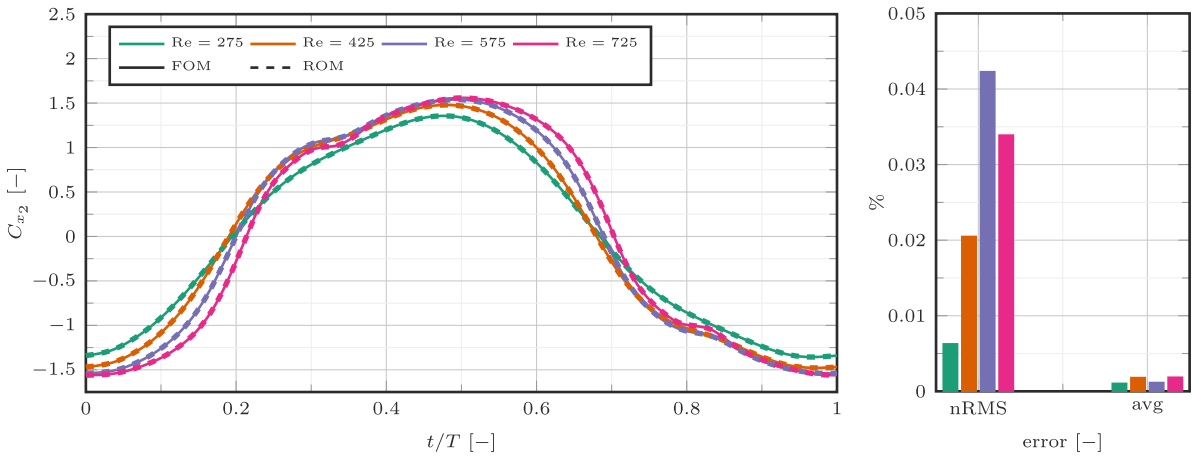

Fig. 13. Reynolds number study: Vertical force coefficient C_{x_2} and corresponding normalized RMS error and absolute error of the average force for reduced-order w.r.t. full-order model.

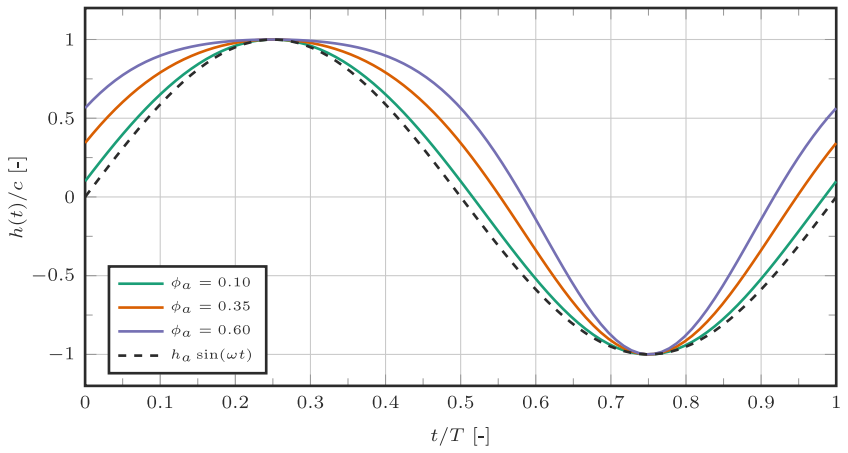

Fig. 14. Motion profile study: Non-sinusoidal heave function as in (41).

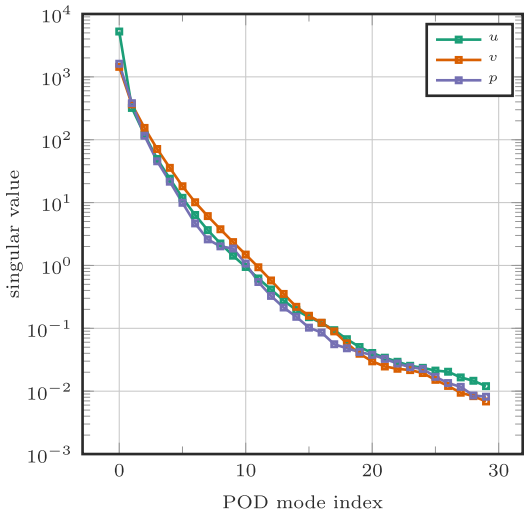

Fig. 15. Motion profile study: Decay of singular values σ_i associated with $\mathbf{V}$.

We create a reduced-order model for a variation of the phase amplitude $0.1 \leq \phi_a \leq 0.6$. The other parameters are chosen similarly to the previous test cases, that is: the Reynolds number is $\mathrm{Re} = 800$, the Strouhal number is $St = 0.125$ and a motion amplitude of $h_a/c = 0.5$.

The singular values σ_i of the snapshot matrix are given in Fig. 15. The steep decrease in the singular values indicates that the problem is amenable to model-order reduction. We assess the reduced-order model at

$$\phi_a \in [0.1625, 0.2875, 0.4125, 0.5375]. \tag{42}$$

These values do not match the amplitudes used for generating the snapshots. We compare the reduced-order model against the full-order model, which is considered as ground truth.

Fig. 16 shows similar trends when comparing the relative error (33) of the variable fields for the reduced-order model versus the full-order model as the previous cases. The errors are the smallest for u_1 and the largest for p. All errors are $\leq \mathcal{O}(0.1\%)$.

Figs. 17 and 18 show very good agreement between the force coefficients computed by the full-order and reduced-order models. The normalized root mean square error (36) and the normalized error of the average (35) are $< 0.01\%$ for C_{x_1} and $< 0.005\%$ for C_{x_2}.

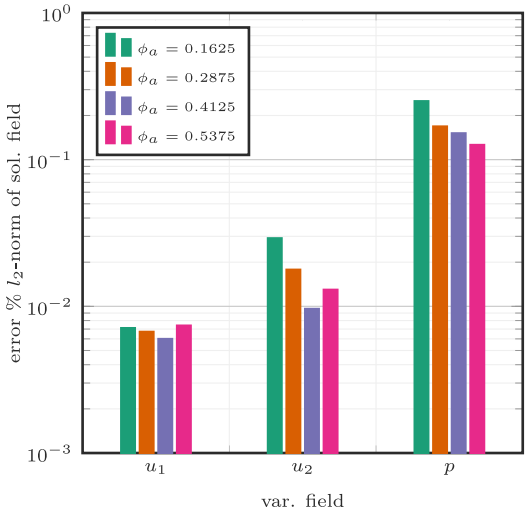

Fig. 16. Motion profile study: l_2-norm of the error ϵ_x (33) of reduced-order w.r.t. full-order model normalized with the l_2-norm of the solution field .

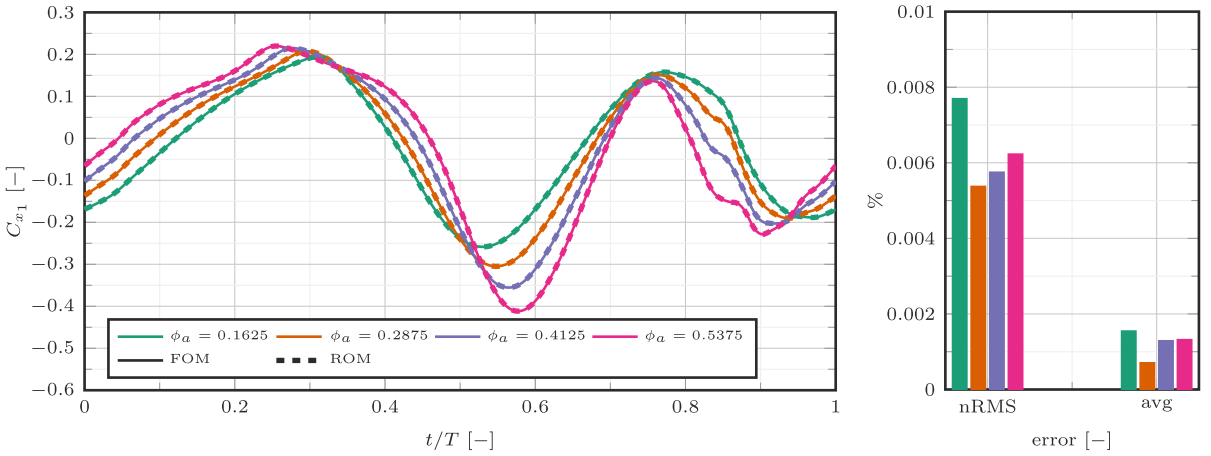

Fig. 17. Motion profile study: Horizontal force coefficient C_{x_1} and corresponding normalized RMS error and absolute error of the average force for reduced-order w.r.t. full-order model.

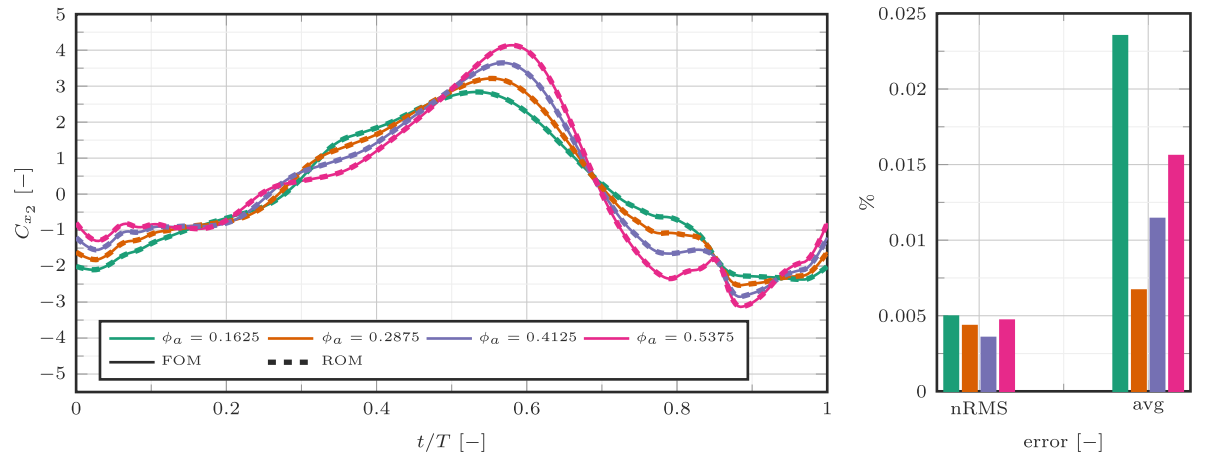

Fig. 18. Motion profile study: Horizontal force coefficient C_{x_2} and corresponding normalized RMS error and absolute error of the average force for reduced-order w.r.t. full-order model.

4. Conclusions

We have successfully implemented a time-periodic reduced-order model. We confirmed the favourable performance of the reduced-order model on the problem of a moving hydrofoil, where we varied the Strouhal number, Reynolds number and heave motion profile.

The computed solution fields of the reduced-order model and full-order model show good agreement. The same is true for the postprocessed forces. While reducing the dimension of the problem from $\mathcal{O}(10^6)$ to $\mathcal{O}(10^2)$ the errors in the force are less than 0.2% for drag and lift. This makes the reduced-order model suitable for computations of a wide variety of time-periodic flows.

The reduced-order model behaved predictably as increasing the size of the reduced basis caused the errors to converge to zero. The reduced-order model offers a speed-up of $\mathcal{O}(10^2)$ - $\mathcal{O}(10^3)$ over the full-order model, depending on the basis size. Higher speed-ups are likely possible when appropriate non-linear reduction techniques, such as hyper-reduction, would be adopted.

Looking forward, there are several interesting avenues for future work. First, extending the model to three spatial dimensions would significantly enhance its applicability. Second, additional verification for higher Reynolds numbers makes the model suitable for more industrial applications. Finally, applying the model to industrial contexts, such as optimizing the performance and layout of wind farms or ship propellers, provides an opportunity to bridge the gap between the ideas in this work and practical solutions.

CRediT authorship contribution statement

Jacob E. Lotz: Writing – original draft, Visualization, Validation, Software, Methodology, Investigation, Formal analysis, Data curation, Conceptualization. **Gabriel D. Weymouth:** Writing – original draft, Supervision, Investigation. **Ido Akkerman:** Writing – original draft, Supervision, Software, Methodology, Investigation, Funding acquisition, Conceptualization.

Declaration of competing interest

The authors declare the following financial interests/personal relationships which may be considered as potential competing interests: Ido Akkerman reports financial support was provided by Dutch Research Council. Jacob E. Lotz reports financial support was provided by Dutch Research Council. If there are other authors, they declare that they have no known competing financial interests or personal relationships that could have appeared to influence the work reported in this paper.

Data availability

Data will be made available on request.

Acknowledgements

This publication is part of the project Lift Control for Hydrofoil Craft (with project number TWM. BL.019.009) of the research programme Top Sector Water & Maritime: The Blue Route which is (partly) financed by the Dutch Research Council (NWO), The Netherlands. This support is gratefully acknowledged.

Appendix A. Temporal and spatial discretization

The spatial convergence for a steady-state case of a foil section at an angle of attack of 3° is given in Fig. A.19. The convergence orders of C_{x_1} and C_{x_2} are 1.3 and 1.4, respectively. A spatial discretization of $h/h_0 = 0.5$ was chosen, as it exhibited errors of 3.0% and 1.1% with the Richardson extrapolated results, offering a balance between computational costs and discretization error. In this discretization the patches are refined to 68 control points between the foil section and the inflow boundary, 62 control points over the length of the foil section and 78 control points between the foil section and the outflow boundary. The spacing of the control points is similar as in [9]. The resulting spatial discretization is visualized in Fig. A.20

The temporal domain was discretized with 49 control points. For a further refinement, the added computational costs do not balance the reduction in error on a pure heaving test case.

Appendix B. Visualization of the basis

In Fig. B.21 visualizes four slices of the shapes of the two most dominant modes of the time-periodic basis. The slices are taken at $t = 0$, $t = \frac{1}{4}T$, $t = \frac{2}{4}T$, $t = \frac{3}{4}T$ for u_1, u_2 and p.

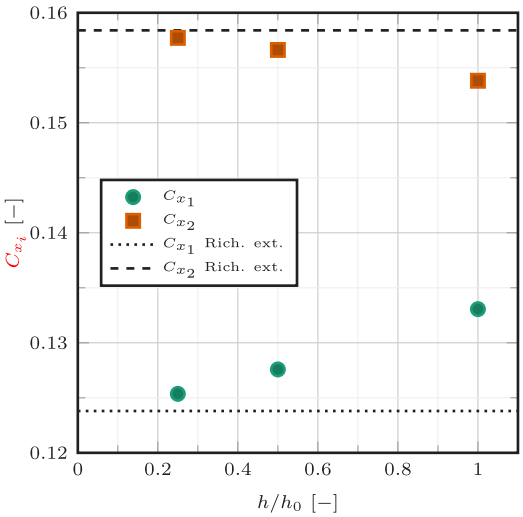

Fig. A.19. Numerical results and Richardson extrapolation of the steady-state force coefficients C_{x_i}. The order of convergence is 1.30 and 1.35 for directions x_1 and x_2 respectively.

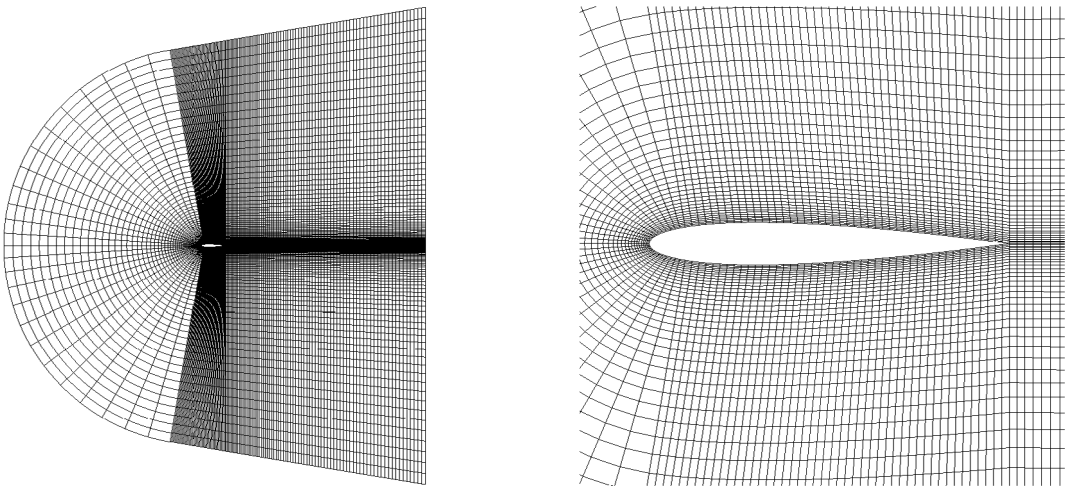

Fig. A.20. Slices of the space–time mesh, showing the discretization of the spatial domain at $t = 0$. Visualized using VisIt [49].

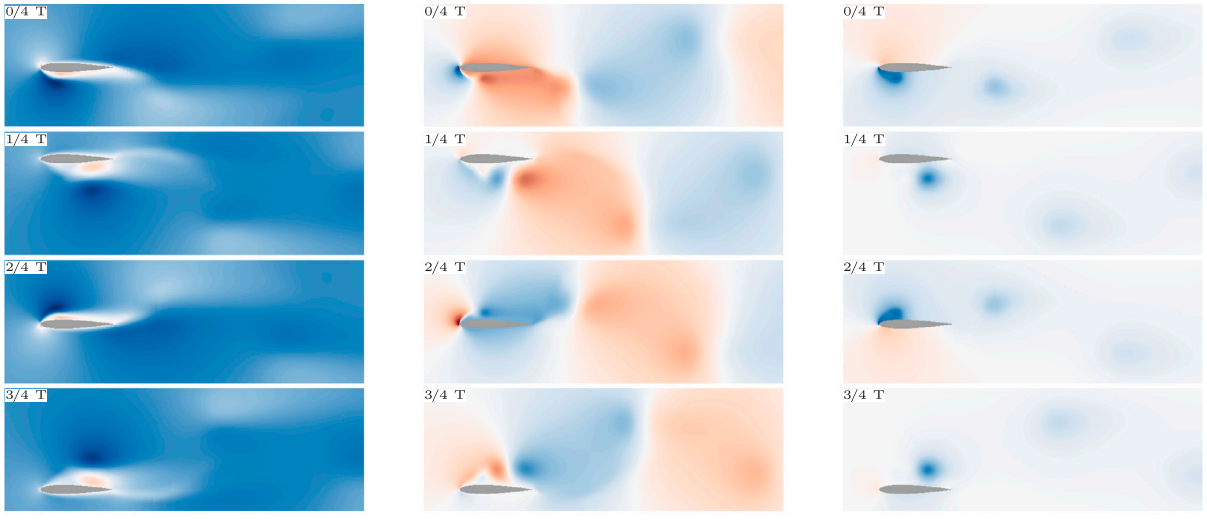

(a) u_1 mode 1 (b) u_2 mode 1 (c) p mode 1

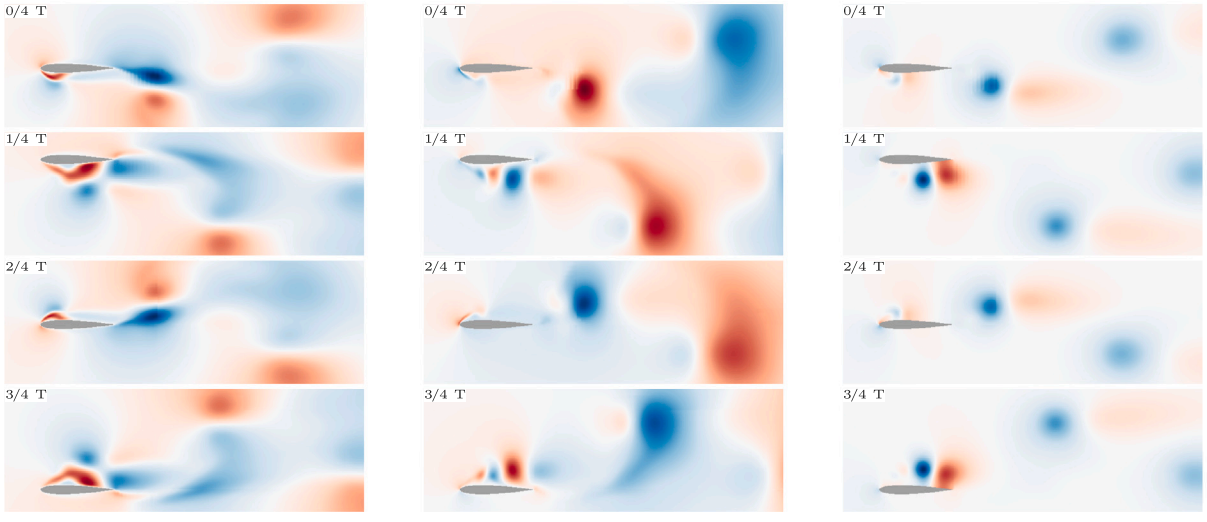

(d) u_1 mode 2 (e) u_2 mode 2 (f) p mode 2

Fig. B.21. Strouhal number study: slices of the first two modes of the basis for u_1, u_2 and p at $t = 0$, $t = \frac{1}{4}T$, $t = \frac{2}{4}T$, $t = \frac{3}{4}T$ showing the shape of the basis. Visualized using VisIt [49].

References

[1] D. Roose, K. Lust, A. Champneys, A. Spence, A Newton-Picard shooting method for Ccmputing periodic solutions of large-scale dynamical systems, Chaos Solitons Fracrals 5 (1995) 1913–1925.
[2] L. Jiang, L.T. Biegler, V.G. Fox, Simulation and optimization of pressure-swing adsorption systems for air separation, AIChE J. 49 (2003) 1140–1157.
[3] T. Richter, An averaging scheme for the efficient approximation of time-periodic flow problems, Comput. & Fluids 214 (2021).
[4] K.C. Hall, J.P. Thomas, W.S. Clark, Computation of unsteady nonlinear flows in cascades using a harmonic balance technique, AIAA J. 40 (2002) 879–886.
[5] A.K. Gopinath, A. Jameson, Time spectral method for periodic unsteady computations over two- and three- dimensional bodies, in: 43rd AIAA Aerospace Sciences Meeting and Exhibit - Meeting Papers, American Institute of Aeronautics and Astronautics Inc., 2005, pp. 10683–10696.
[6] V.K. Gupta, S.K. Bhatu, Solution of cyclic profiles in catalytic reactor operation with periodic flow reversal, Comput. Chem. Eng. 15 (1991) 229–237.
[7] A.G. Salinger, G. Eigenberger, The direct calculation of period states of the reversible flow reactor - I. Methodology and propane combustion results, Chem. Eng. Sci. 51 (1996) 4903–4913.
[8] F. Platte, D. Kuzmin, C. Fredebeul, S. Turek, Novel simulation approaches for cyclic steady-state fixed-bed processes exhibiting sharp fronts and shocks, in: Trends and Applications in Constructive Approximation, 2005, pp. 207–223.
[9] J.E. Lotz, M.F.P. Ten Eikelder, I. Akkerman, Space-time computations of exactly time-periodic flows past hydrofoils, Comput. & Fluids 277 (2024) 106286.
[10] G. Stabile, F. Ballarin, G. Zuccarino, G. Rozza, A reduced order variational multiscale approach for turbulent flows, Adv. Comput. Math. 45 (2019) 2349–2368.
[11] S. Grimberg, C. Farhat, N. Youkilis, On the stability of projection-based model order reduction for convection-dominated laminar and turbulent flows, J. Comput. Phys. 419 (2020).

[12] A.E. Løvgren, Y.M., E.M. Rønquist, A reduced basis element method for the steady stokes problem, Math. Modelling Numer. Anal. 40 (2006) 529–552.
[13] I. Akhtar, A.H. Nayfeh, C.J. Ribbens, On the stability and extension of reduced-order Galerkin models in incompressible flows: AAA numerical study of vortex shedding, Theor. Comput. Fluid Dyn. 23 (2009) 213–237.
[14] S. Lorenzi, A. Cammi, L. Luzzi, G. Rozza, POD-Galerkin method for finite volume approximation of Navier–Stokes and RANS equations, Comput. Methods Appl. Mech. Engrg. 311 (2016) 151–179.
[15] A. Caiazzo, T. Iliescu, V. John, S. Schyschlowa, A numerical investigation of velocity-pressure reduced order models for incompressible flows, J. Comput. Phys. 259 (2014) 598–616.
[16] B.R. Noack, P. Papas, P.A. Monkewitz, The need for a pressure-term representation in empirical Galerkin models of incomrpressible shear flows, J. Fluid Mech. 523 (2005) 339–365.
[17] E. Fonn, H. van Brummelen, T. Kvamsdal, A. Rasheed, Fast divergence-conforming reduced basis methods for steady Navier–Stokes flow, Comput. Methods Appl. Mech. Engrg. 346 (2019) 486–512.
[18] G. Rozza, D.B.P. Huynh, A. Manzoni, Reduced basis approximation and a posteriori error estimation for Stokes flows in parametrized geometries: Roles of the inf-sup stability constants, Numer. Math. 125 (2013) 115–152.
[19] F. Ballarin, A. Manzoni, A. Quarteroni, G. Rozza, Supremizer stabilization of POD-Galerkin approximation of parametrized steady incompressible Navier-Stokes equations, Internat. J. Numer. Methods Engrg. 102 (2015) 1136–1161.
[20] G. Stabile, G. Rozza, Finite volume POD-Galerkin stabilised reduced order methods for the parametrised incompressible Navier–Stokes equations, Comput. & Fluids 173 (2018) 273–284.
[21] A. Ivagnes, G. Stabile, A. Mola, T. Iliescu, G. Rozza, Pressure data-driven variational multiscale reduced order models, J. Comput. Phys. 476 (2023).
[22] T. Iliescu, Z. Wang, Variational multiscale proper orthogonal decomposition: Navier-stokes equations, Numer. Methods Partial Differential Equations 30 (2014) 641–663.
[23] T.C. Rebollo, E.D. Ávila, M.G. Marmol, F. Ballarin, G. Rozza, On a certified smagorinsky reduced basis turbulence model, SIAM J. Numer. Anal. 55 (2017) 3047–3067.
[24] Z. Wang, I. Akhtar, J. Borggaard, T. Iliescu, Proper orthogonal decomposition closure models for turbulent flows: A numerical comparison, Comput. Methods Appl. Mech. Engrg. 237–240 (2012) 10–26.
[25] Y. Bazilevs, V.M. Calo, J.A. Cottrell, T.J.R. Hughes, A. Reali, G. Scovazzi, Variational multiscale residual-based turbulence modeling for large eddy simulation of incompressible flows, Comput. Methods Appl. Mech. Engrg. 197 (1–4) (2007) 173–201.
[26] R. Reyes, R. Codina, Projection-based reduced order models for flow problems: A variational multiscale approach, Comput. Methods Appl. Mech. Engrg. 363 (2020).
[27] A. Tello, R. Codina, J. Baiges, Fluid structure interaction by means of variational multiscale reduced order models, Internat. J. Numer. Methods Engrg. 121 (2020) 2601–2625.
[28] R. Codina, R. Reyes, J. Baiges, A posteriori error estimates in a finite element VMS-based reduced order model for the incompressible Navier-Stokes equations, Mech. Res. Commun. 112 (2021).
[29] S. Buoso, A. Manzoni, H. Alkadhi, V. Kurtcuoglu, Stabilized reduced-order models for unsteady incompressible flows in three-dimensional parametrized domains, Comput. & Fluids 246 (2022).
[30] S. Hijazi, G. Stabile, A. Mola, G. Rozza, Data-driven POD-Galerkin reduced order model for turbulent flows, J. Comput. Phys. 416 (2020).
[31] C. Mou, B. Koc, O. San, L.G. Rebholz, T. Iliescu, Data-driven variational multiscale reduced order models, Comput. Methods Appl. Mech. Engrg. 373 (2021).
[32] X. Xie, C. Webster, T. Iliescu, Closure learning for nonlinear model reduction using deep residual neural network, Fluids 5 (2020).
[33] J. Baiges, R. Codina, I. Castañar, E. Castillo, A finite element reduced-order model based on adaptive mesh refinement and artificial neural networks, Internat. J. Numer. Methods Engrg. 121 (2020) 588–601.
[34] O. San, S. Pawar, A. Rasheed, Variational multiscale reinforcement learning for discovering reduced order closure models of nonlinear spatiotemporal transport systems, Sci. Rep. 12 (2022).
[35] T.J.R. Hughes, J.A. Cottrell, Y. Bazilevs, Isogeometric analysis: CAD, finite elements, NURBS, exact geometry and mesh refinement, Comput. Methods Appl. Mech. Engrg. 194 (2005) 4135–4195.
[36] Y. Bazilevs, I. Akkerman, Large eddy simulation of turbulent Taylor–Couette flow using isogeometric analysis and the residual-based variational multiscale method, J. Comput. Phys. 229 (9) (2010) 3402–3414.
[37] T.J.R. Hughes, M. Mallet, M. Akira, A new finite element formulation for computational fluid dynamics: II. Beyond SUPG, Comput. Methods Appl. Mech. Engrg. 54 (3) (1986) 341–355.
[38] M.F.P. ten Eikelder, I. Akkerman, Variation entropy: a continuous local generalization of the TVD property using entropy principles, Comput. Methods Appl. Mech. Engrg. 355 (2019) 261–283.
[39] M.F.P. ten Eikelder, Y. Bazilevs, I. Akkerman, A theoretical framework for discontinuity capturing: Joining variational multiscale analysis and variation entropy theory, Comput. Methods Appl. Mech. Engrg. 359 (2020) 112664.
[40] R. Anderson, J. Andrej, A. Barker, J. Bramwell, J.S. Camier, J. Cerveny, V. Dobrev, Y. Dudouit, A. Fisher, T. Kolev, W. Pazner, M. Stowell, V. Tomov, I. Akkerman, J. Dahm, D. Medina, S. Zampini, MFEM: A modular finite element methods library, Comput. Math. Appl. 81 (2021) 42–74.
[41] A.J. Chorin, Numerical solution of the Navier-Stokes equations, Math. Comp. 22 (104) (1968) 745–762.
[42] R. Témam, Sur l'approximation de la solution des équations de Navier-Stokes par la méthode des pas fractionnaires (I), Arch. Ration. Mech. Anal. 32 (2) (1969) 135–153.
[43] A.J. Chorin, A numerical method for solving incompressible viscous flow problems, J. Comput. Phys. 135 (2) (1997) 118–125.
[44] hypre, *hypre*: High Performance Preconditioners. https://llnl.gov/casc/hypre https://github.com/hypre-space/hypre.
[45] J.L. Lumley, The structure of inhomogeneous turbulent flows, in: Atmospheric Turbulence and Radio Wave Propagation, Nauka, 1967.
[46] Y. Choi, W. Arrighi, D. Copeland, R. Anderson, G. Oxberry, libROM, 2019, http://dx.doi.org/10.11578/dc.20190408.3, Computer Software.
[47] T. Kvamsdal, K.M. Okstad, Error estimator for variational consistent surface forces in Navier-Stokes simulations, in: Proceedings for Computational Mechanics, New Trends and Applications, CIMNE, Barcelona, Spain, 1998, pp. 1–11.
[48] H. Melbø, T. Kvamsdal, Goal oriented error estimators for Stokes equations based on variationally consistent postprocessing, Comput. Methods Appl. Mech. Engrg. 192 (2002).
[49] H. Childs, E. Brugger, B. Whitlock, J. Meredith, S. Ahern, D. Pugmire, K. Biagas, M. Miller, C. Harrison, G.H. Weber, H. Krishnan, T. Fogal, A. Sanderson, C. Garth, E.W. Bethel, D. Camp, O. Rübel, M. Durant, J.M. Favre, P. Navrátil, VisIt: An end-user tool for visualizing and analyzing very large data, in: High Performance Visualization–Enabling Extreme-Scale Scientific Insight, 2012, pp. 357–372.